LAWRENCE
LIVERMORE
NATIONAL
LABORATORY

LLNL-TR-817068

Multichannel Deconvolution of Vibrational Shock Signals: An Inverse Filtering Approach

J. V. Candy, K. A. Fisher, B. A. Markowicz, D. J. Paulsen

November 24, 2020

Disclaimer

This document was prepared as an account of work sponsored by an agency of the United States government. Neither the United States government nor Lawrence Livermore National Security, LLC, nor any of their employees makes any warranty, expressed or implied, or assumes any legal liability or responsibility for the accuracy, completeness, or usefulness of any information, apparatus, product, or process disclosed, or represents that its use would not infringe privately owned rights. Reference herein to any specific commercial product, process, or service by trade name, trademark, manufacturer, or otherwise does not necessarily constitute or imply its endorsement, recommendation, or favoring by the United States government or Lawrence Livermore National Security, LLC. The views and opinions of authors expressed herein do not necessarily state or reflect those of the United States government or Lawrence Livermore National Security, LLC, and shall not be used for advertising or product endorsement purposes.

This work performed under the auspices of the U.S. Department of Energy by Lawrence Livermore National Laboratory under Contract DE-AC52-07NA27344.

Multichannel Deconvolution of Vibrational Shock Signals: An Inverse Filtering Approach

J. V. Candy, K. A. Fisher, B. A. Markowicz, D. J. Paulsen

1 INTRODUCTION

When transporting critical systems of national security interest, out-of-the ordinary, impulsive-events that can potentially be undetected and affect overall system performance are of great concern. Impulsive events that can occur are essentially pulse-like, transient signals of short duration that evolve from various phenomena. Here the event can be created by either the dropping of a test object, the system, subjecting it to a compact high-energy blow or being struck unintentionally during transit resulting in potential damage. The intensity and location of the strike can cause an inoperability condition that is unacceptable in a national security environment. Therefore, it is essential to detect, classify and localize damage of any test object subjected to an impulsive-event.

This effort was targeted to evaluate the vibrational response of test objects that are subjected to "transport" shocks and roadway vibrations during shipping and handling. Any potential damage that could be inflicted during transportation must not only be detected, but also be evaluated to determine the operational readiness of a test object before and after transport. This event is a critical task that must be addressed as part of the Lawrence Livermore National Laboratory (*LLNL*) national security mission.

The estimation of excitation signals from noisy data is termed the deconvolution problem in the signal processing literature. The *deconvolution problem* is based on recovering the input excitation signal from a system characterized by its impulse response sequence [1]-[5]. Using this model of the system, an "inverse" representation or filter is developed to remove the system from the measured data and recover the input [6]-[7]. Deconvolution techniques have existed for a long-time; however, transient deconvolution presents a few uncommon problems, since the signal has a finite-length time duration resulting in a limited amount of data containing information about the excitation process. The transient is wide-band in the frequency domain relative to any measurement sensor implying that the smaller bandwidth sensor system "filters" the excitation eliminating some of its essential information for recovery. This fact, coupled with the filtering effect of the test object itself makes this excitation recovery (deconvolution) problem a challenge for signal processing.

Deconvolution is a problem that has been investigated for a long period of time whether it is attempting to locate a seismic source or ocean acoustic target or speaker in a crowded hall or extracting an explosive source for analysis [2], [3], [10], [11]. This problem is even more exasperated when multiple signals are involved—a situation prevalent in array based systems [13]. Multichannel deconvolution poses a myriad of issues besides the fundamental one that it is an ill-posed "inverse" problem [8]-[12]. Many techniques resort to first obtaining the multichannel impulse response and the apply it channel-by-channel to perform the deconvolution using a single channel method (e.g. Wiener deconvolution [10], [14]). Assuming that the system under investigation is lightly coupled, then this approach can be effective. However, when the system is tightly coupled, such as in a vibrating structure, then the single channel approach can lead to erroneous excitation estimates.

There are two viable candidate approaches that can be used to mitigate this multichannel problem. The first is the well-known Wiener least-squares solution employing the nonparametric multichannel Levinson algorithm developed by Robinson [1], [2]. The second approach incorporates a state-space model that can be used to develop and inverse filter directly from input/output data. This approach incorporates any existing coupling of modes that exists in the underlying structure being monitored. That is, the state-space approach is to estimate the response of an underlying linear time-invariant, multichannel structural system using a black-box state-space model. This model captures the underlying structural dynamics of critical components enabling a viable vibration analysis to ensure that even weakly coupled modal signals buried in the noise are represented. The structural test object is a mechanical system that is modeled by a coupled multichannel mass-damper-spring (*MCK*) structure that characterizes its response to an impulsive-event shock pulse excitation illustrating the approach. First, the multichannel *MCK*-system model in state-space form is discussed followed by the methodology to extract it from noisy experimental data using a shaping or inverse filter design [15], [16].

We start by investigating the structure of the multichannel impulse response and then show how the state-space easily captures its internal structure. That is, the impulse response is an input/output description of a system under investigation with its Fourier transform yielding the corresponding multichannel transfer function (matrix), while the input/state/output state-space construct enables the internal structure of a system with all of its coupling to be revealed as well as the input/output response.

We start by investigating the structure of the multichannel impulse response of a multichannel mechanical structural test object captured by a linear, time-invariant, *MCK*-system [15] and then show how the state-space easily captures this multiple input/multiple output (*MIMO*) representation in Sec. 1. That is, the impulse response is an input/output description of a system under investigation with its Fourier transform yielding the corresponding multichannel transfer function (matrix), while the input/state/output state-space construct enables the internal structure of a system with all of its coupling to be revealed as well as the input/output response.

Next we define the basic problem and investigate various transient shock signals that typically occur during transit. Using a simple *MCK*-model of a vibrating structure developed in Sec. 2 [15] various sets of noisy data are synthesized for each individual excitations using the well-known Gauss-Markov representation [14] in Sec. 3. multichannel deconvolution problem is discussed in Sec. 4 from the *MIMO* construct for both impulse response and transfer function representations and extended to incorporate state-space models [14]. Shaping or inverse filter designs for multichannel deconvolution using the state-space approach is discussed in Sec. 5 and applied to the individual excitation data sets. This is followed by applications of this approach in Sec. 6, first to noisy mass-simulation transportation data obtained by transporting a large-mass concrete block using a tractor/tailer vehicle on typical roadways followed by the vibrational response experiment of a test object excited by random excitations for a shaker table experiment completing the study.

2 Vibrational Response Model

Mechanical systems are important in many applications, especially when considering vibrational responses of critical components such as turbine-generator pairs in nuclear systems on ships or even at home as well as aircraft structures that transport people throughout the world. Next we briefly present the generic multivariable mechanical system representation that will be employed in examples and case studies to follow.

Linear, time-invariant multiple input/output (*MIMO*) mechanical systems are characterized by the vector-matrix differential equations that can be expressed as [15]

$$M\ddot{\mathbf{d}}(t) + C_d\dot{\mathbf{d}}(t) + K\mathbf{d}(t) = B_p\mathbf{p}(t) \tag{1}$$

where $\mathbf{d}$ is the $N_d \times 1$ displacement vector, $\mathbf{p}$ is the $N_p \times 1$ excitation force, and M, C_d, K, are the $N_d \times N_d$ lumped mass, damping, and spring constant matrices characterizing the vibrational process model, respectively. The structure of these matrices, typically, take the form as

$$M = \begin{bmatrix} M_1 & 0 & 0 & 0 & 0 \\ 0 & M_2 & 0 & 0 & 0 \\ \vdots & \vdots & \ddots & \vdots & \vdots \\ 0 & 0 & 0 & M_{N_d-1} & 0 \\ 0 & 0 & 0 & 0 & M_{N_d} \end{bmatrix}, \qquad C_d = \begin{bmatrix} C_{d_{ij}} \end{bmatrix}, \quad \text{and}$$

$$K = \begin{bmatrix} (K_1+K_2) & -K_2 & 0 & 0 & 0 \\ -K_2 & (K_2+K_3) & \ddots & 0 & 0 \\ 0 & \ddots & \ddots & -K_{N_d-1} & 0 \\ 0 & 0 & -K_{N_d-1} & (K_{N_d-1}+K_{N_d}) & -K_{N_d} \\ 0 & 0 & 0 & -K_{N_d} & K_{N_d} \end{bmatrix}$$

If we define the $2N_d$-state vector as $\mathbf{x}(t) := \left[\ \mathbf{d}(t) \ \mid \ \dot{\mathbf{d}}(t)\ \right]'$, then the continuous-time state-space representation of this process can be expressed as

$$\dot{\mathbf{x}}(t) \;=\; \underbrace{\begin{bmatrix} 0 & | & I \\ --- & | & --- \\ -M^{-1}K & | & -M^{-1}C_d \end{bmatrix}}_{A} \mathbf{x}(t) + \underbrace{\begin{bmatrix} 0 \\ --- \\ M^{-1}B_p \end{bmatrix}}_{B} \mathbf{p}(t) \tag{2}$$

The corresponding measurement or output vector relation can be characterized by

$$\mathbf{y}(t) = \mathbf{C_a}\ddot{\mathbf{d}}(t) + \mathbf{C_v}\dot{\mathbf{d}}(t) + \mathbf{C_d}\mathbf{d}(t) \tag{3}$$

where the constant matrices: $\mathbf{C_a}, \mathbf{C_v}, \mathbf{C_d}$ are the respective acceleration, velocity and displacement weighting matrices of appropriate dimension.

In terms of the state vector relations of Eq. 2, we can express the acceleration vector as:

$$\ddot{\mathbf{d}}(t) = -M^{-1}K\mathbf{d}(t) - M^{-1}C_d\dot{\mathbf{d}}(t) + M^{-1}B_p\mathbf{p}(t) \tag{4}$$

Substituting for the acceleration term in Eq. 3, we have that

$$\mathbf{y}(t) = -\mathbf{C_a}M^{-1}\Big[B_p\mathbf{p}(t) - C_d\dot{\mathbf{d}}(t) - K\mathbf{d}(t)\Big] + \mathbf{C_v}\dot{\mathbf{d}}(t) + \mathbf{C_d}\mathbf{d}(t)$$

or

$$\mathbf{y}(t) = \underbrace{\Big[C_d - \mathbf{C_a}M^{-1}K \;\;|\;\; \mathbf{C_v} - \mathbf{C_a}M^{-1}\mathbf{C_d}\Big]}_{C} \begin{bmatrix} \mathbf{d}(t) \\ --- \\ \dot{\mathbf{d}}(t \end{bmatrix} + \underbrace{\mathbf{C_a}M^{-1}B_p}_{D}\,\mathbf{p}(t) \tag{5}$$

to yield the vibrational measurement as:

$$\mathbf{y}(t) = C\mathbf{x}(t) + D\mathbf{u}(t) \tag{6}$$

where the output or measurement vector is $\mathbf{y} \in \mathcal{R}^{N_y \times 1}$ completing the multiple input/multiple output (*MIMO*) vibrational model. The is the form of the model to be identified directly from the data, that is, the model set is represented by $\Sigma_{ABCD} = \{A, B, C, D\}$.

Corresponding to this representation is the discrete *transfer function* matrix in terms of the $\mathcal{Z}$-transform

$$\mathcal{H}(z) = C(zI - A)^{-1}B + D \tag{7}$$

with the corresponding *impulse response* matrix specified by its set of Markov parameters $(\{CA^{t-1}B + D\delta(t)\})$ specified by the underlying state-space model [14], [16]

$$\mathcal{H}(t) = \underbrace{CA^{t-1}B + D}_{\text{Markov Parameters}}\;\delta(t) \tag{8}$$

Recall that the *Z-transform* ($\mathcal{Z}$) is the discrete-time equivalent of the Laplace transform (S) for continuous-time systems and is related through the *impulse invariant transformation* given by $\mathcal{Z} = e^{\mathcal{S}\triangle T}$. The corresponding *discrete Fourier transform* (DFT) pair is defined by

$$\begin{aligned} Y(z)\Big|_{z=e^{j\Omega_m}} = Y(\Omega_m) := DFT\Big[y(t)\Big] &= \sum_{t=0}^{M-1} y(t)e^{-j\Omega_m t} \\ y(t) = IDtFT\Big[Y(\Omega_m)\Big] &= \frac{1}{M}\sum_{t=0}^{M-1} Y(\Omega_m)e^{j\Omega_m t} \end{aligned} \tag{9}$$

similar to the continuous Fourier transform calculated on the $j\omega$-axis, the DFT is calculated on the unit circle in the $\mathcal{Z}$-domain [14].

In order to utilize information about the acoustic object of interest and validate approaches to recover the excitation, a typical structural test object of interest is employed to extract a reasonable model for simulation and analysis. The approach taken was to use a multichannel method to extract the shock excitation from synthesized calibration-type data ensuring a reasonable representation of the overall system and enabling a capability to analyze algorithm performance. Next we investigate a simple mechanical system in [15] that will be incorporated in processor design and analysis.

Consider the simple 3-mass (spring-damper) mechanical system[1] illustrated in Fig. 1 from [15] where $m_i = 1; k_i = 3, k_4 = 0;$ and $d_i = 0.01k_i, d_4 = 0; i = 1, \cdots, 3$. These parameters along with the input/output transmission matrices lead to the following state-space representation ($N_x = 6, N_u = 1, N_y = 3$).

$$\begin{aligned} \ddot{\mathbf{x}}(t) &= A\mathbf{x}(t) + B\mathbf{u}(t) \\ \mathbf{y}(t) &= C\mathbf{x}(t) + D\mathbf{u}(t) \end{aligned}$$

$$A = \left[\begin{array}{ccc|ccc} 0 & 0 & 0 & 1 & 0 & 0 \\ 0 & 0 & 0 & 0 & 1 & 0 \\ 0 & 0 & 0 & 0 & 0 & 1 \\ - & - & - & - & - & - \\ -6 & 3 & 0 & -0.06 & 0.03 & 0 \\ 3 & -6 & 3 & 0.03 & -0.06 & 0.03 \\ 0 & 3 & -3 & 0 & 0.03 & -0.03 \end{array}\right]; B = \begin{bmatrix} 0 \\ 0 \\ 0 \\ 0 \\ 0 \\ 1 \end{bmatrix}; C = \left[\begin{array}{ccc|ccc} 1 & 0 & 0 & 0 & 0 & 0 \\ 0 & 0 & 0 & 1 & 0 & 0 \\ 0 & 0 & 0 & 0 & 0 & 1 \end{array}\right]$$

with $D = 0$.

[1]See [15] for a detailed analysis of this mechanical system.

Exciting this system with an impulse yields the 3-output response shown in Fig. 2 along with its accompanying Fourier spectra. Discretizing the response with a sampling interval of $\triangle t = 0.01 sec$ shows the 6^{th}-order system $(N_d = 3, N_x = 6)$ with modal frequencies determined from the "discrete" system matrix that is transformed from the discrete (z-domain) to the continuous (s-domain)—($\mathcal{Z} \rightarrow \mathcal{S}$) given by

$$s = \frac{1}{\triangle t} \ln z$$

to yield the modal frequencies at: $\{p_i = 0.497Hz, 0.343Hz, 0.123Hz\}$ corresponding to the peaks present in the Fourier transform of Fig. 2. These features that make this structural model interesting from a processing perspective is that it can represent any number of mechanical objects or sensors such as displacement, velocity or acceleration measurements that occur routinely in vibrational monitoring systems.

We can consider this representation a simple set of object/sensor measurements that are contaminated with random disturbances and noise leading to a stochastic system that incorporates the dynamic *MCK*-model along with Gaussian noise sources. This stochastic problem leads to a *Gauss-Markov* state-space model with noise sources assumed zero-mean, Gaussian, with covariance matrices, $\mathbf{R}_{vv}(t)$ and $\mathbf{R}_{ww}(t)$, respectively (see Fig. 14a for internal structure). In this case, the discrete state equations become:

$$\begin{aligned} \mathbf{x}(t+1) &= A\mathbf{x}(t) + B\mathbf{u}(t) + \mathbf{w}(t) && \text{[State]} \\ \mathbf{y}(t) &= C\mathbf{x}(t) + D\mathbf{u}(t) + \mathbf{v}(t) && \text{[Measurement]} \end{aligned} \tag{10}$$

that becomes the basis of the deconvolution problems to follow.

For the constant state and noise covariances Π, R_{ww}, R_{wv} and R_{vv}, the *stationary measurement covariance* at lag ℓ is:

$$\Lambda_{yy}(\ell) = CA^{\ell-1}\left(A\Pi(\ell)C' + R_{wv}(\ell)\right) \qquad \ell = 0, 1, \cdots, N$$

to complete the description.

If a deterministic *SVD* realization (identification) technique was performed using the impulse response or covariance data at a high *SNR* of 50 dB. The rank of the Hankel matrix from the *SVD* decomposition indicates a 6^{th}-order system (3-modes) as observed in Fig. 3(a). The realization results are shown in Fig. 3(b)-(d) where we see the modal frequency estimates that match those of the system closely along with the estimated channel outputs overlaid onto the raw impulse response data—again indicating an accurate realization due to the high *SNR*. In Fig. 3(b) we compare the estimated average power spectra from the *SVD* realization of the model to the 3-output spectra and show the location of the extracted modal frequencies. Note how all of the peaks align indicating a valid realization of the underlying

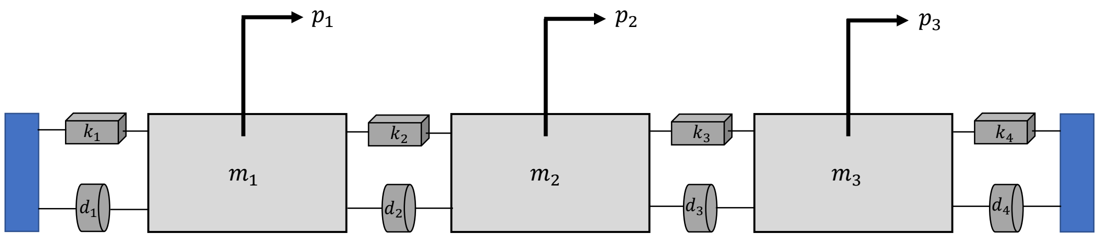

Figure 1: The 3-output mechanical system under investigation.

mechanical system. The pole-zero representation along with the extracted modal frequencies are shown in Fig. 3(c).

Thus, we have a mechanical *MCK*-system that will be used to synthesized "sensor" data useful to evaluate the performance of potential single/multichannel deconvolution techniques to follow by incorporating multiple inputs (excitations) representing a variety of transient shock pulses.

3 IMPACT PROBLEM: Excitation Signal Analysis

In this section, the various components of the Impact Problem are discussed leading to a synthesis of data enabling an analysis of the basic problem as well as providing an eventual simulation test bed for the development of signal processing techniques that can be applied to each of the facets of this problem [17]. To synthesize a data set essential components of the problem must be identified individually. As illustrated in Fig. 4 the data initiated by an impulsive-event is characterized by an impulse-like pulse that excites the vibrational response of the particular structural object that is then measured by the sensor system. The response as well as the sensors are subjected to uncertainties and noise as illustrated by additive sources contaminating the object as well as the sensor responses. Therefore, the overall synthesis of this model is concerned with: (1) impulsive-event shock pulse; (2) vibrational

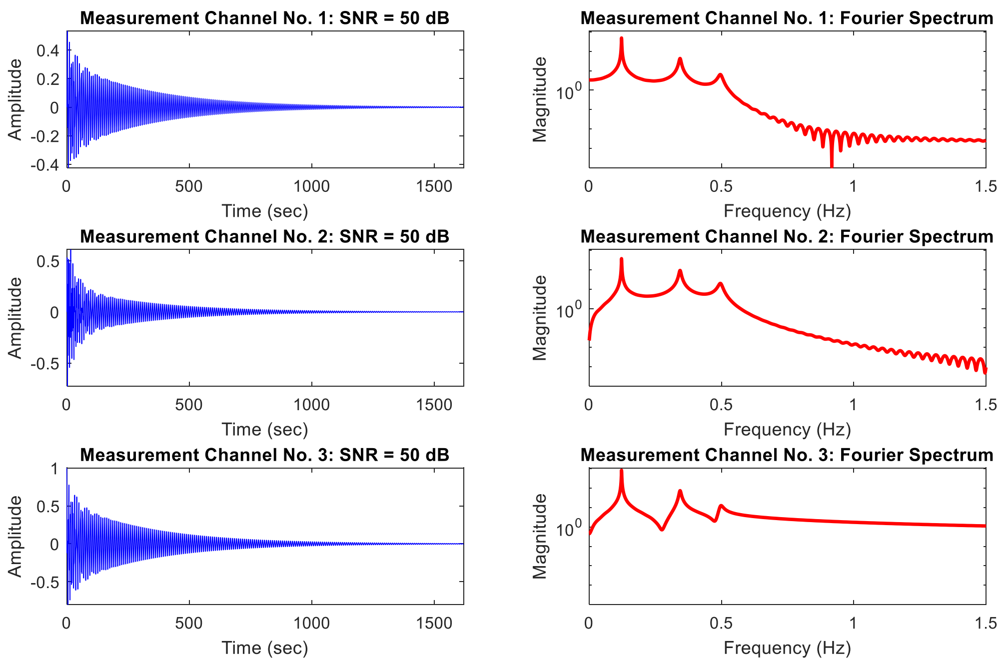

Figure 2: Impulse response and spectrum of 3-output mechanical system. (a) Synthesized channel impulse responses. (b) Fourier transforms of channel responses with spectral peaks at: $0.497Hz, 0.343Hz, 0.123Hz$.

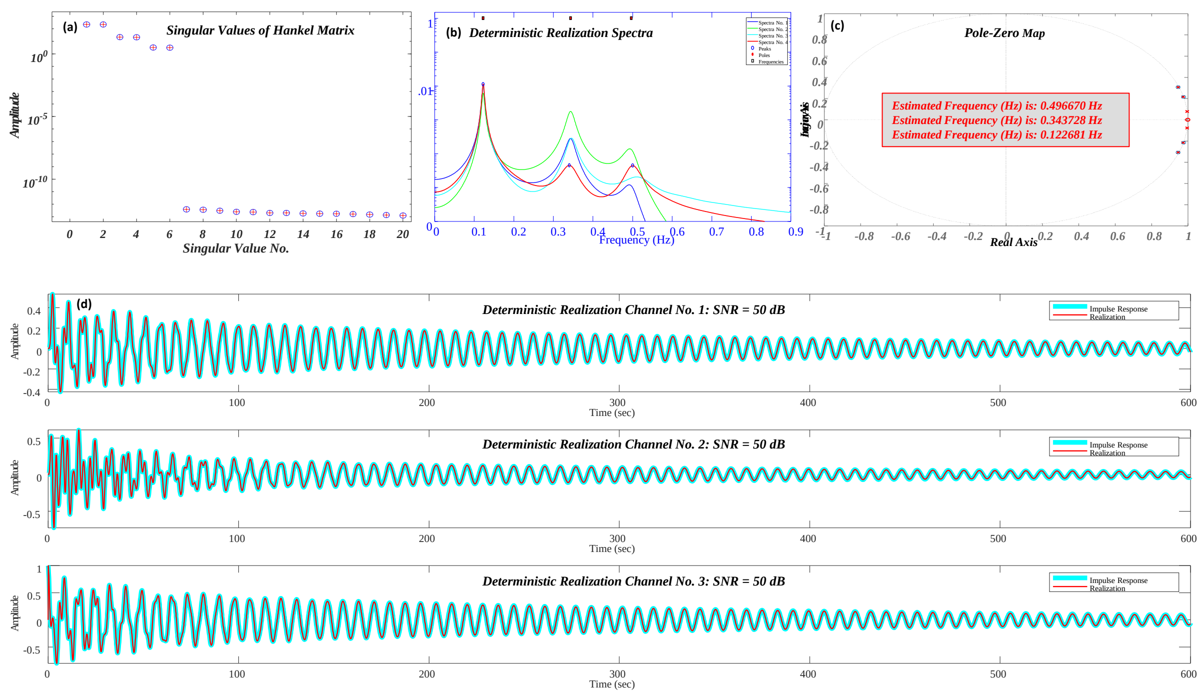

Figure 3: *SVD* realization of 3-output mechanical system. (a) Singular values of the Hankel matrix. (b) Power spectra: outputs/average with poles (boxes). (c) Frequencies with poles/zeros. (d) Realization output channels (data/realization) overlays.

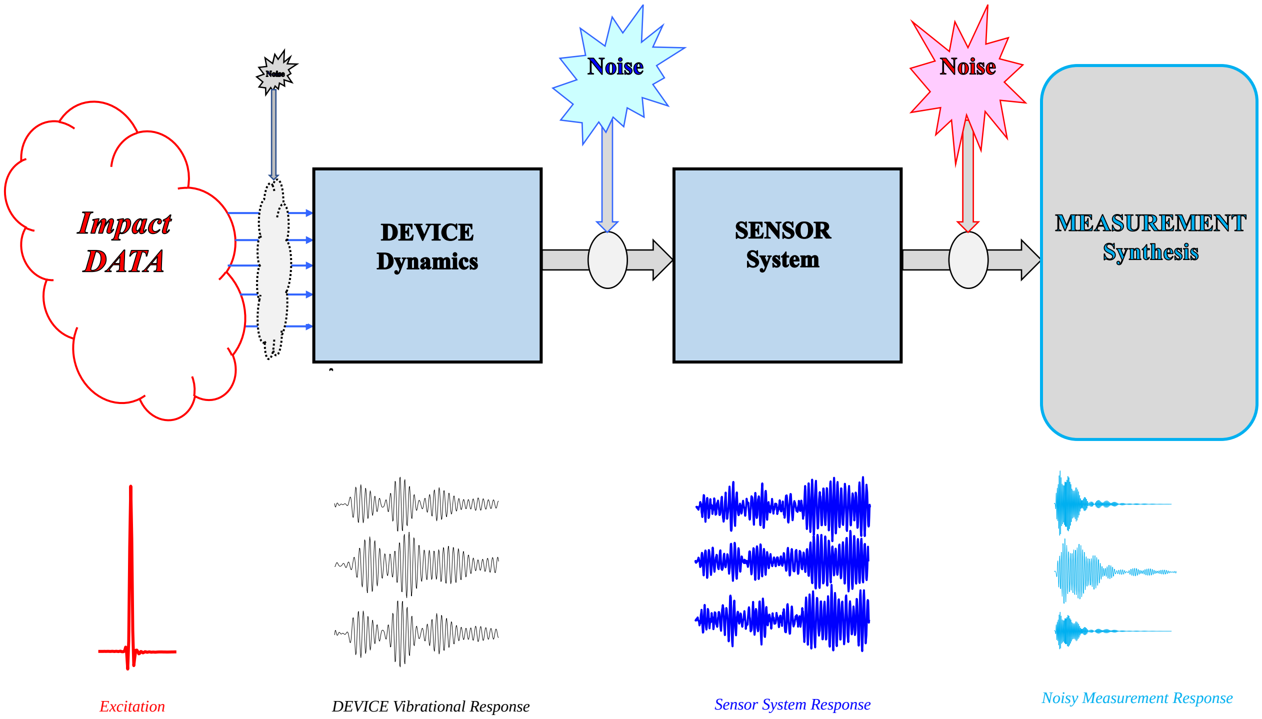

Figure 4: Multichannel Impact Problem showing the data generated by the impulsive-event exciting the test object generating its vibrational response contaminated with noise then measured by the sensor instrumentation system also contaminated by instrumentation as well as environmental noise providing a realistic measurement system output.

dynamics of the structural object; and (3) sensor system response—all contaminated with uncertainties and noise.

A variety of excitations can occur during shipping and handling for transport. Initially, we consider hammer-strikes that can occur at any time during this process followed by three typical excitations: [18]

- *HAMMER*—a hammer-strike can impact the structural test object and is employed during calibration testing as well as any sharp blow that can during shipping/handling operations.

- *DROP*—a drop can occur anytime during shipping/handling when the structural object is being placed in a container or trailer.

- *HAZARD*—a hazard can occur anytime during transit, once the object is placed in the transporter (truck, train, plane, ship, etc.).

- *ROAD*—a road induced vibration can occur anytime during transit on a roadway or rail or at sea/air.

These are the primary shocks that will be considered in this study. First, we analyze each excitation individually and then apply them to our problem.

3.1 Excitation: Hammer-Strike

In this subsection, the properties of a typical hammer strike applied to a structural test object are investigated in order to ascertain what, if any, unique properties exist that can be exploited for detection and recovery. A set of instrumented hammer-strikes was obtained from a previous test. An ensemble of 12-strikes were recorded and their corresponding spectra shown in Fig. 5a. The ensemble spectra indicate that the frequency is relatively flat out to $3.2KHz$–the Nyquist sampling frequency. An average hammer-strike pulse is shown in Fig. 5b along with its corresponding spectrum. It appears to roll-off out to $3.2KHz$ with a reasonably flat spectrum out to $1.2KHz$—a good band covering the frequency range of interest for the object. It is interesting that the raw pulse data appears relatively symmetrical and Gaussian-like in structure as observed in Fig. 5a. It is also interesting to note that both the amplitude and pulse width are reasonably fixed over the ensemble. Unfortunately a direct pulse measurement data is not feasible, since the overall structural object response, environment, and noise must also be included leading to the required multichannel deconvolution approach to follow. A spectrogram (frequency vs time vs magnitude) using a recursive-in-time technique (see Appendix C for details) of the average hammer-strike is shown in Fig. 6 indicating a concentration of energy across the entire frequency band synthesizing an impulse-like excitation. A dominant peak at approximately $100Hz$ is shown in the ensemble spectrum (green) and histogram (red) as well.

3.2 Excitation: DROP

The DROP is the most severe of excitations that can be directly applied to the structural object being transported. It can occur in a variety of situations when the object is being handled for shipping such as: forklift placement or moving the object through a variety of transporters (e.g. truck-to-train or truck-to-plane). Raw median DROP data (blue) are shown in Fig. 7(a) along with the corresponding spectra. Here the data were obtained using tri-axial accelerometers and pre-processed (filtered, trends removed, decimated) to mitigate the measurement noise. This data were provided as input to a subspace identification processor (10-mode, 20-th order) to capture its major frequency content as shown in Fig. 7(b) with the raw (turquoise) and identified (red-filled) spectra indicated along with corresponding frequency peaks (list inset). From the figure it is clear that the estimator has captured a viable representation of a DROP event excitation, since both low and high frequencies are extracted. To see this even further a spectrogram (frequency vs time vs energy) was estimated for both the raw and identified excitations with the results shown in Fig. 8 respectively along with the time series (red) ensemble spectra (green) and frequency peak histogram (red). From the raw data shown in (a), it is clear that a variety of noise

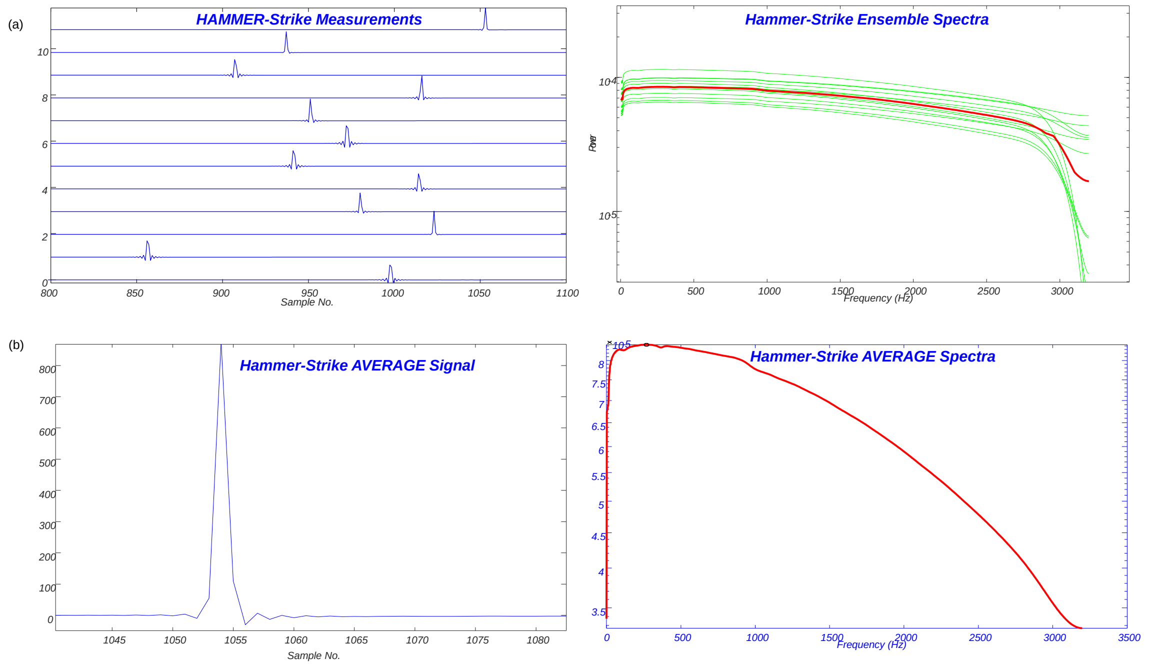

Figure 5: HAMMER-Strike Data: (a) Ensemble time series and spectra. (b) Average time series and spectrum.

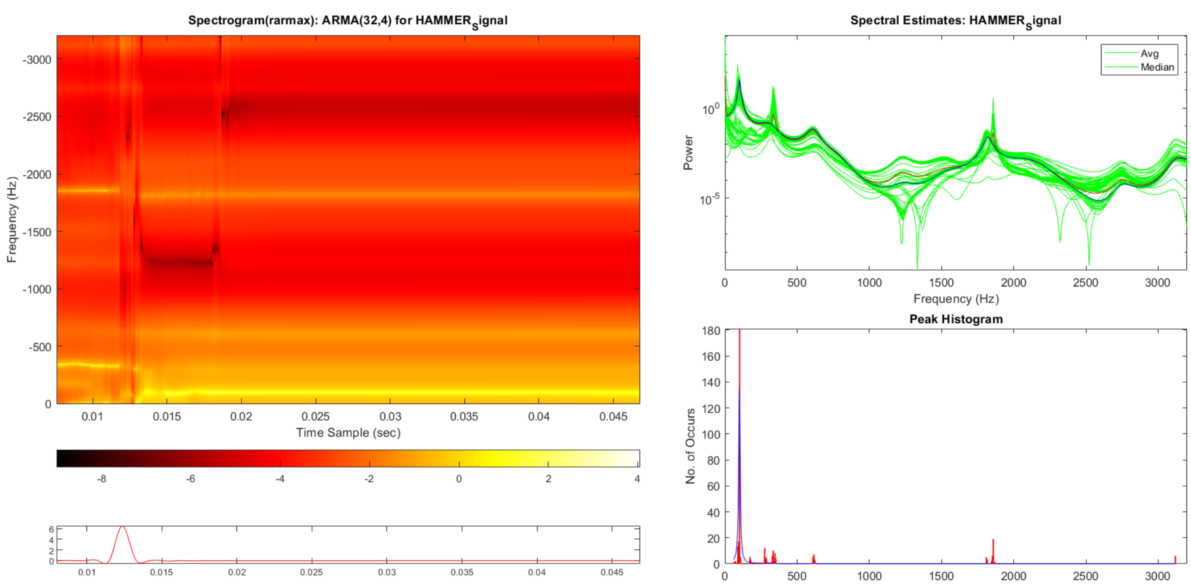

Figure 6: HAMMER Excitation Model Identification Spectrogram Analysis: HAMMER spectrogram, signal (red), ensemble spectra (green) and peak frequency histogram (red).

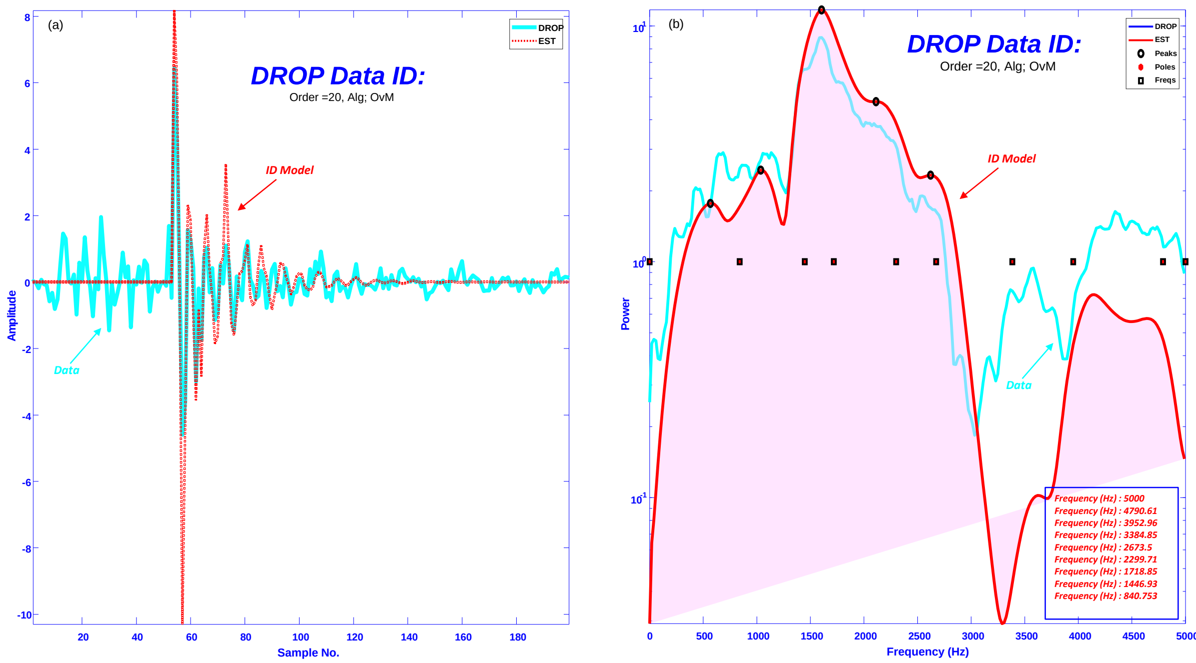

Figure 7: DROP Excitation Model Identification: (a) Raw median data and estimated DROP pulse. (b) Raw median DROP spectrum and estimate (model).

peaks occur, while that of the simplified identification model has captured the major energy while minimizing the noise uncertainty. However, in both spectra, it is clear the this type of excitation excites most frequencies across the entire band. Next we consider the related HAZARD that can occur during transit on the roadway or railway.

3.3 Excitation: HAZARD

The HAZARD excitation can also occur in a variety of manners. For instance, if construction were being performed on a road or railway with uneven surfaces being exposed as well as pot-holes on a road for example. A typical HAZARD excitation is shown in Fig. 9 with the median time series (turquoise), the identified model response (red) in (a) and corresponding spectra (blue) in (b). Again, we see that the simplified model response obtained by the subspace identifier (15-mode, 30-th order) captures a majority of the spectral energy (red-filled) as shown in (b). The corresponding HAZARD spectrogram analysis is shown in Fig. 10 where we observe the high frequencies dominated by the noise in (a) and mitigated by the identifier in (b). It is clear that the frequency peaks are well-defined as indicated by the corresponding ensemble spectra (green) and peak histogram (red). Finally we consider, perhaps the most prevalent excitation, vibrational response due to damaged or repairing surfaces.

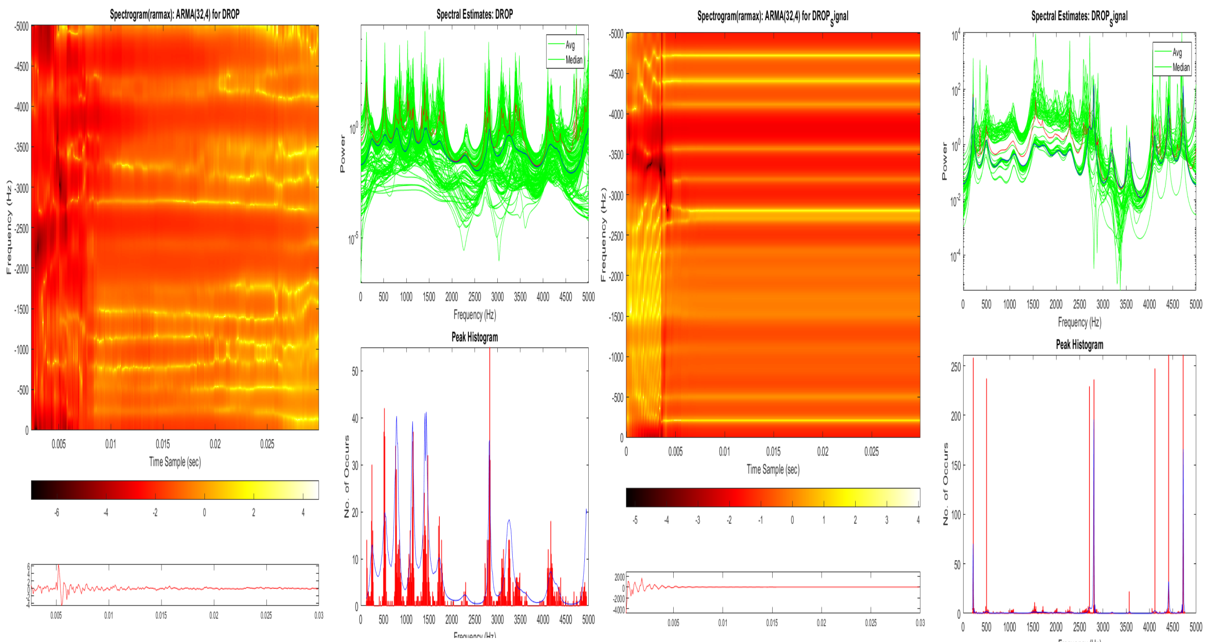

Figure 8: DROP Excitation Model Identification Spectrogram Analysis: DROP spectrogram, signal (red), ensemble spectra (green) and peak frequency histogram (red). (a) Raw DROP data. (b) DROP model data.

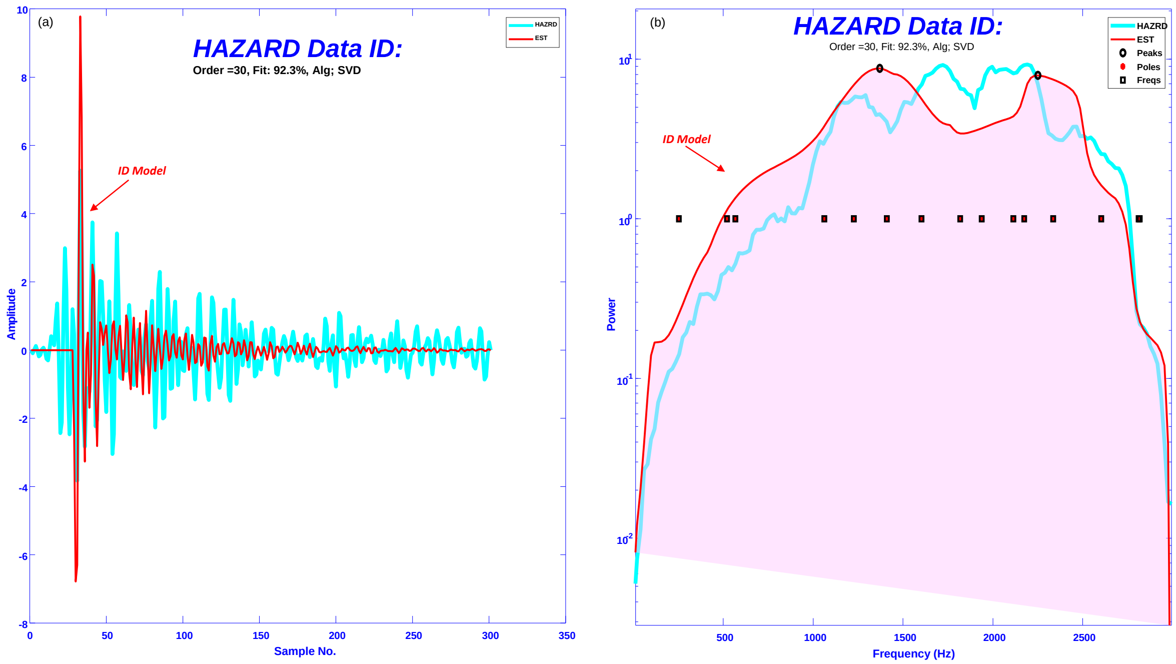

Figure 9: HAZARD Excitation Model Identification: (a) Raw median data (turquoise) and estimated HAZARD pulse (red). (b) Raw median HAZARD spectrum (turquoise) and model estimate (red-filled).

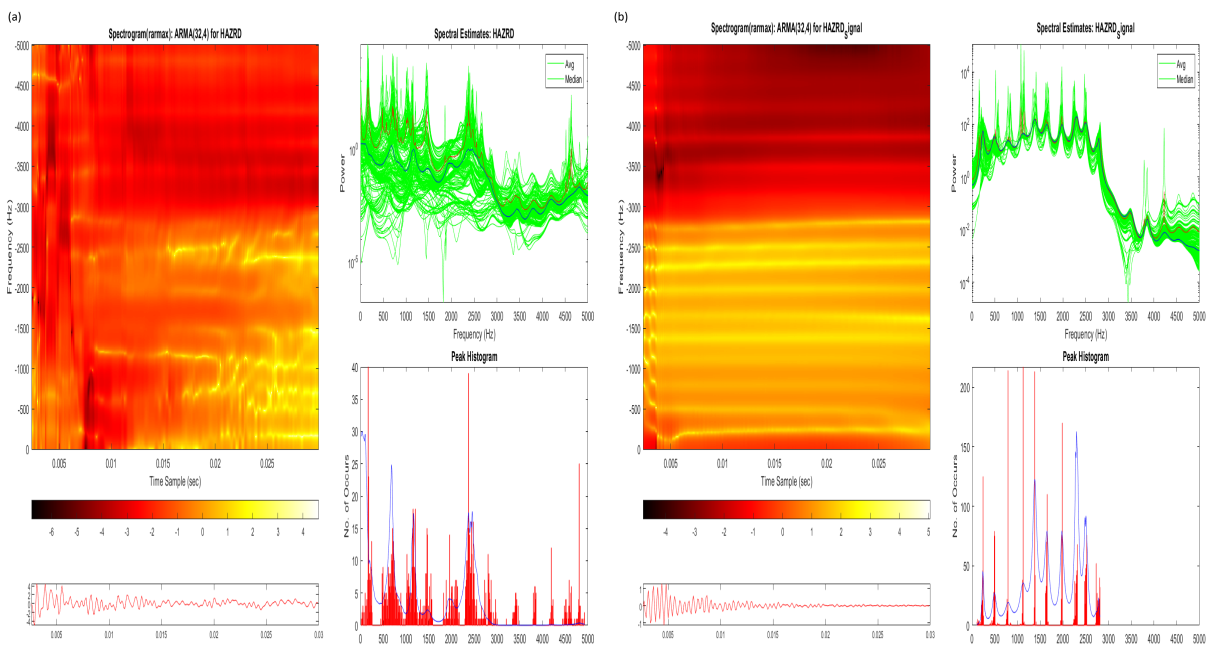

Figure 10: HAZARD Excitation Model Identification Spectrogram Analysis: HAZARD spectrogram, signal (red), ensemble spectra (green) and peak frequency histogram (red). (a) Raw HAZARD data. (b) HAZARD model data.

3.4 Excitation: ROAD

The ROAD excitation induces a persistent vibrational response of the transported structural object during transit. It is typically caused by rough surfaces resulting in uneven road and railways. The typical ROAD excitation is shown in Fig. 11 with the median time series (turquoise), the identified model (20-mode, 40-th order)) response (red) in (a) and corresponding spectra in (b). In this case, the median roadway vibration data (turquoise) data is quite noisy, while the identified model data (red) mitigates much of these uncertainties. Comparing the median measured accelerometer spectrum with that of the model (red-filled) spectrum provided by the subspace algorithm (see Appendix A), it is clear that this simplified representation has captured the extended frequency spectrum. The corresponding spectrum confirms this premise with the median time series (red) providing a noisy uncertain spectral ensemble (green), while that produced by the identified much simpler with much less uncertainty. Finally, the corresponding spectrograms illustrating the raw and modeled spectral information is shown in Fig. 12.

Summarizing, the variety of excitation measurements were simplified using the subspace identification processor providing an archive of such signals for eventual simulation and analysis. A comparison of the DROP, HAZARD and ROAD spectral are shown in Fig. 13 indicating that each they cover the frequency band extensively from $0.1 - 3.2KHz$ with the exception of the HAZARD shock pulse that only extends up to $2KHz$ and then rolls off rapidly. This completes the excitation suite that will be applied to our transportation problem.

4 Multichannel Deconvolution

The basic deterministic deconvolution problem can be defined mathematically as:

GIVEN an N_y-vector measurement sequence $\{\mathbf{y}(t)\}; t = 1, \cdots, N_t$ for $\mathbf{y} \in \mathcal{R}^{N_y \times 1}$, FIND the corresponding N_u-vector excitation (input) sequence, $\{\mathcal{U}(t)\}$

The direct solution to the deterministic deconvolution problem is given by

$$\underbrace{\mathcal{U}(t)}_{\text{Excitation}} = \underbrace{\mathcal{H}^{-1}(t)}_{\text{Inverse Impulse Response}} \star \underbrace{\mathbf{y}(t)}_{\text{Measurement}} \tag{11}$$

or in the $\mathcal{Z}$-domain as

$$\underbrace{\mathcal{U}(z)}_{\text{Excitation}} = \underbrace{\mathcal{H}^{-1}(z)}_{\text{Inverse Transfer Function}} \times \underbrace{\mathbf{Y}(z)}_{\text{Measurement}} \tag{12}$$

Therefore, it is clear mathematically why this problem is termed an “inverse” problem—primarily because the system impulse response matrix or transfer function must be inverted

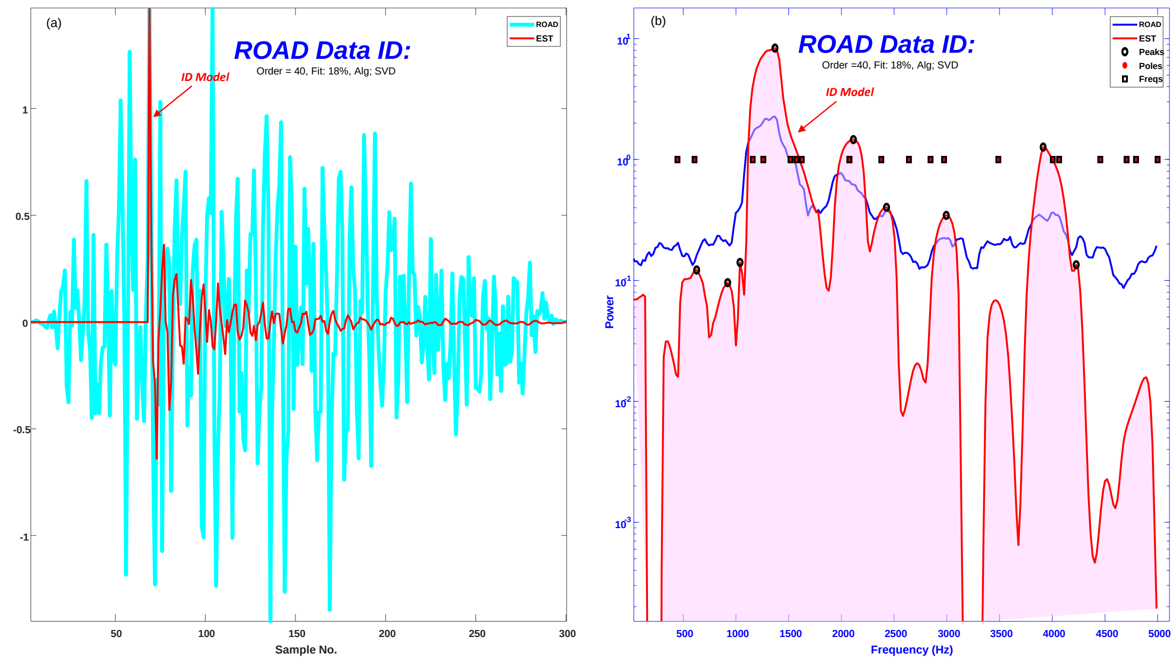

Figure 11: ROAD Excitation Model Identification: (a) Raw median data (turquoise) and estimated ROAD pulse (red). (b) Raw median ROAD spectrum (turquoise) and model estimate (red-filled).

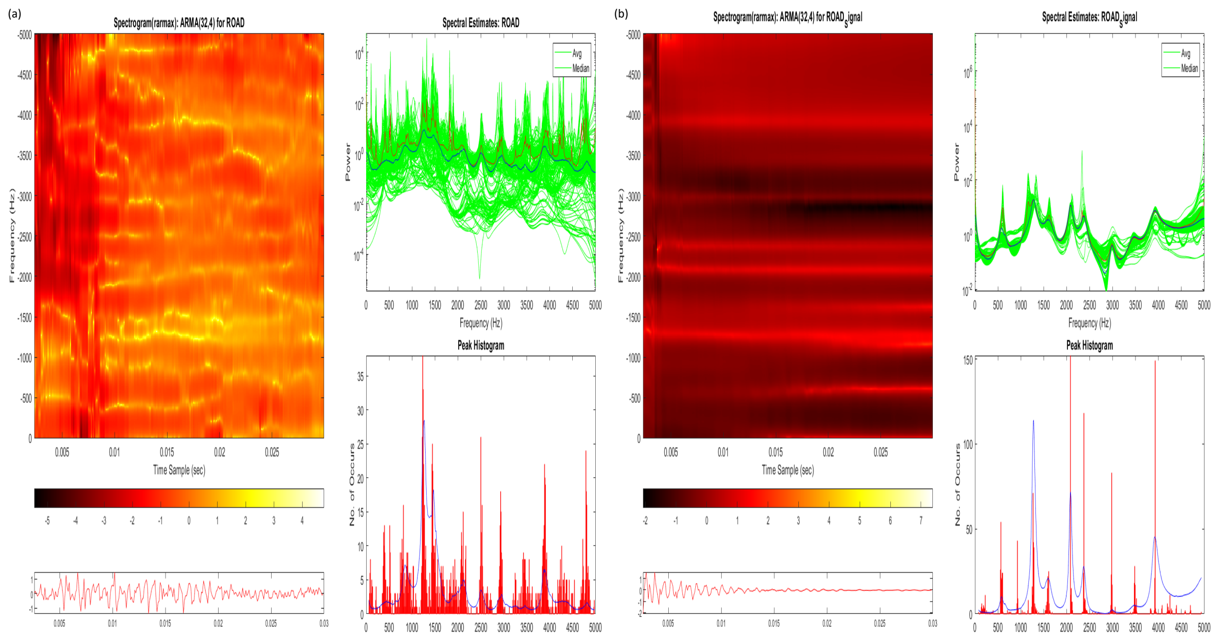

Figure 12: ROAD Excitation Model Identification Spectrogram Analysis: ROAD spectrogram, signal (red), ensemble spectra (green) and peak frequency histogram (red). (a) Raw ROAD data. (b) ROAD model data.

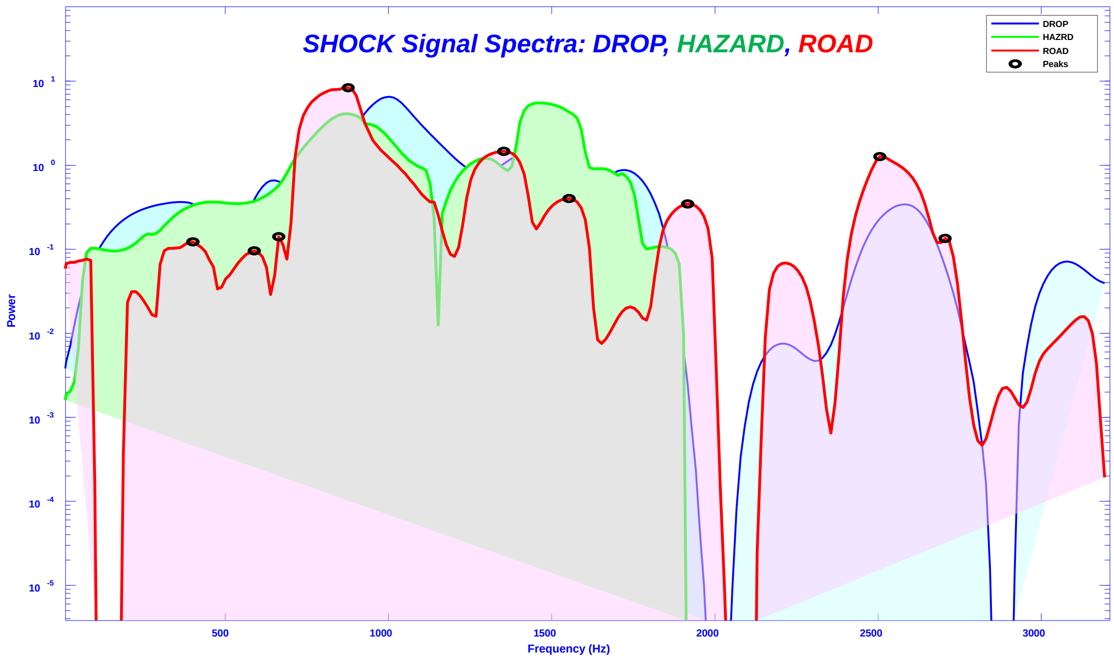

Figure 13: DROP, HAZARD, ROAD Excitation Model Comparisons: DROP (blue), HAZARD (green) and ROAD (red).

in order to recover the excitation signal. Approaches to solve the deconvolution problem range from a simple division of Fourier spectra to more sophisticated Wiener inversions using smoothed power spectra to achieve reasonable results for the single channel case [14]. However, all attempts in the multichannel case usually result in transfer function modeling approaches and time domain solutions as in the seismic case [2]. For multichannel acoustic systems, a state-space model is one of the fundamental mechanisms applicable [8], [9], [17].

The multiple channel models can be developed, starting with a set of input/output representations eventually leading to a set of *deterministic* state-space models. Typical *discrete-time* deterministic multiple input/multiple output (*MIMO*) systems can be characterized by their impulse response matrices or equivalently multichannel transfer function matrices. The impulse response of a discrete-time system is

$$\mathbf{y}(t) = \mathcal{H}(t) \star \mathbf{u}(t) = \sum_{k=0}^{K} \mathcal{H}(t-k)\mathbf{u}(k) \tag{13}$$

with t is the discrete-time index, $\star$ the multichannel *convolution* operator and $\mathbf{y} \in \mathrm{R}^{N_y \times 1}$, the vector of outputs, $\mathbf{u} \in \mathrm{R}^{N_u \times 1}$, the vector of inputs, $\mathcal{H} \in \mathrm{R}^{N_y \times N_u}$ the *impulse response matrix.*

The corresponding discrete transfer function, $\mathcal{H}(z)$ is characterized by the input/output relation

$$\mathbf{Y}(z) = \mathcal{H}(z) \times \mathbf{U}(z) \tag{14}$$

with the *discrete-time* transfer function matrix defined by $\mathcal{H}(z)$.

The impulse response can be represented as a multichannel matrix in terms of its inputs (columns) and outputs (rows) or equivalently in terms of column vector functions ($\mathbf{h}_i(t) \in \mathcal{R}^{N_y} \times 1$) or row vector functions ($\mathbf{h}_i^T(t) \in \mathcal{R}^{N_u} \times 1$), that is,

$$\mathcal{H}(t) = \text{Outputs} \underbrace{\left\{ \begin{bmatrix} h_{11}(t) & \cdots & h_{1N_u}(t) \\ \vdots & \ddots & \vdots \\ h_{N_y1}(t) & \cdots & h_{N_yN_u}(t) \end{bmatrix} \right\}}_{\text{Inputs}} = [\mathbf{h}_1(t) \mid \cdots \mid \mathbf{h}_{N_u}(t)] = \begin{bmatrix} \mathbf{h}_1^T(t) \\ --- \\ \vdots \\ --- \\ \mathbf{h}_{N_y}^T(t) \end{bmatrix} \tag{15}$$

The multichannel convolution operations are then defined in terms of this representation as:

$$\mathbf{y}(t) = \mathcal{H}(t) \star \mathbf{u}(t) = [\mathbf{h}_1(t) \mid \cdots \mid \mathbf{h}_{N_u}(t)] \star \mathbf{u}(t) = [\mathbf{h}_1(t) \star \mathbf{u}(t) \mid \cdots \mid \mathbf{h}_{N_u}(t) \star \mathbf{u}(t)] \tag{16}$$

and therefore,

$$\begin{aligned} \mathbf{y}(t) = \mathcal{H}(t) \star \mathbf{u}(t) &= \begin{bmatrix} h_{11}(t) \star u_1(t) & \cdots & h_{1N_u}(t) \star u_{N_u}(t) \\ \vdots & \ddots & \vdots \\ h_{N_y1}(t) \star u_1(t) & \cdots & h_{N_yN_u}(t) u_{N_u}(t) \end{bmatrix} \\ &= \begin{bmatrix} \sum_{k=0}^{K} h_{11}(k) u_1(t-k) & \cdots & \sum_{k=0}^{K} h_{1N_u}(k) u_{N_u}(t-k) \\ \vdots & \ddots & \vdots \\ \sum_{k=0}^{K} h_{N_y1}(k) u_1(t-k) & \cdots & \sum_{k=0}^{K} h_{N_yN_u}(k) u_{N_u}(t-k) \end{bmatrix} \end{aligned} \tag{17}$$

where $h_{mn}(t)$ the impulse response from the n-th input excitation ($u_n(t)$) measured at the m-th output channel ($y_m(t)$); for $m = 1, \cdots, N_y$; and $n = 1, \cdots, N_u$.

The multichannel transfer function matrix is obtained by applying the $\mathcal{Z}$-transform to obtain

$$\mathcal{H}(z) = \begin{bmatrix} H_{11}(z) & \cdots & H_{1N_u}(z) \\ \vdots & \ddots & \vdots \\ H_{N_y1}(z) & \cdots & H_{N_yN_u}(z) \end{bmatrix} = [\mathbf{H}_1(z) \cdots \mathbf{H}_{N_u}(z)] \quad \text{for} \quad \mathbf{H}_n \in \mathcal{C}^{N_y \times 1} \tag{18}$$

The multichannel system can also be represented in state-space form with the impulse response matrix given in terms of its Markov parameters

$$\mathcal{H}(t) = \underbrace{CA^{t-1}B + D\delta(t)}_{\text{Markov Parameters}}; t = 0, 1, \cdots, N \tag{19}$$

such that

$$\mathcal{H}(t) = \begin{bmatrix} \mathbf{c}_1^T A^{t-1}\mathbf{b}_1 + d_{11}\delta(t) & \cdots & \mathbf{c}_1^T A^{t-1}\mathbf{b}_{N_u} + d_{1N_u}\delta(t) \\ \vdots & \ddots & \vdots \\ \mathbf{c}_{N_y} A^{t-1}\mathbf{b}_1 + d_{N_y 1}\delta(t) & \cdots & \mathbf{c}_{N_y}^T A^{t-1}\mathbf{b}_{N_u} + d_{N_y N_u}\delta(t) \end{bmatrix} \tag{20}$$

with the corresponding transfer function matrix in state-space form given by

$$\mathcal{H}(z) = \begin{bmatrix} \mathbf{c}_1^T (zI-A)^{-1}\mathbf{b}_1 + d_{11} & \cdots & \mathbf{c}_1^T (zI-A)^{-1}\mathbf{b}_{N_u} + d_{1N_u} \\ \vdots & \ddots & \vdots \\ \mathbf{c}_{N_y}^T (zI-A)^{-1}\mathbf{b}_1 + d_{N_y 1} & \cdots & \mathbf{c}_{N_y}^T (zI-A)^{-1}\mathbf{b}_{N_u} + d_{N_y N_u} \end{bmatrix} \tag{21}$$

illustrating the fact that the input/state/output representation captures the input/output as well as the internal structure of the underlying system in terms of its state variables and equivalent impulse response/transfer function matrices.

With this information in mind, the solution to the multichannel deconvolution problem is based on designing and applying an inverse filter to recover the excitation as shown in Eq. 12. A direct model of an inverse filter is quite difficult to obtain analytically; however, we apply a subspace identification technique (*N4SID*) to solve the multichannel deconvolution problem. Essentially, this approach is used to design a "shaping filter" (see [14]) based on the state-space approach using representative excitation signals and apply it directly noisy data. Once designed, the filter is applied to measured data extracting the desired excitation directly.

5 Inverse (Shaping) Filter Design

In order to investigate the state-space approach to the multichannel deconvolution problem, we employ the simple 3-mass mechanical system investigated in the previous section developed by Gawronski [15]. In contrast, we use a 2-input hammer-strike excitation that would be available if the structure was impacted simultaneously by direct forces on the 1-st and 3-rd masses. The linear system in this case is characterized by the usual *MCK*-model dynamics parameterized in the multichannel structure of Eq. 1. As excitations, we incorporate actual hammer-strike transient measurements scaled to this problem and contaminated with random noise. The shaping (inverse) filter is developed to primarily take on input a set of calibration measurement data and on output produce the excitations, that is, the filter is designed to create a filter that estimates the inputs. First, the impulse response of the shaping filter must be estimated and second apply it to measured data as its input. From the deconvolution problem perspective, the shaping filter is the required "inverse filter".

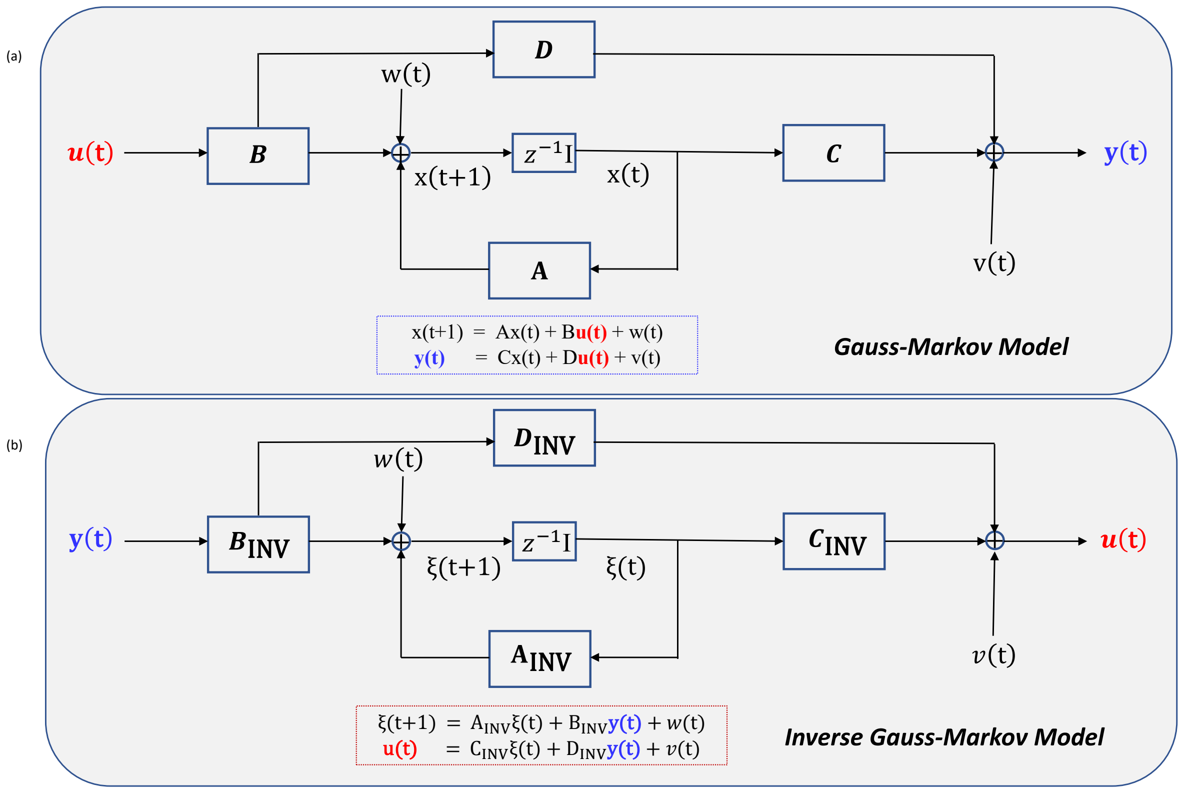

Figure 14: State-Space Realizations of Gauss-Markov and Inverse Filters: (a) Gauss-Markov model: Input: $(\mathbf{u}(t))$ and Output: $(\mathbf{y}(t))$. (b) Inverse Gauss-Markov (shaping) filter: Input: $(\mathbf{y}(t))$ and Output: $(\mathbf{u}(t))$.

In the state-space framework, we have that $\Sigma_{inv} = \{A_{inv}, B_{inv}, C_{inv}, D_{inv}\}$ characterized by

$$
\begin{aligned}
\xi(t+1) &= A_{inv}\xi(t) + B_{inv}\mathbf{y}(t) + w(t) && \text{[State]} \\
\mathbf{u}(t) &= C_{inv}\xi(t) + D_{inv}\mathbf{y}(t) + v(t) && \text{[Excitation]}
\end{aligned} \tag{22}
$$

where $\mathbf{y}$ is the new *input* and $\mathbf{u}$ is the new *output* of this inverse filter "shaping" it to be the actual excitation. as shown in Fig. 14(b).

In summary, the multichannel shaping (inverse) filter *design* procedure is:

- *Obtain* sensor *calibration* data;
- *Extract* transient *excitation* data from archives or experiments;
- *Design* shaping (inverse) filter, $\hat{\Sigma}_{inv} = \{\hat{A}_{inv}, \hat{B}_{inv}, \hat{C}_{inv}, \hat{D}_{inv}\}$, using subspace identification (*N4SID*); and

- *Filter* measured data with the inverse filter to extract the true excitation.

In the *MCK*-problem, we use multichannel hammer-strikes as the desired excitation signal from archive data in a high *SNR*-environment to design the inverse (shaping) filter and then apply it to noisy synthesized noisy accelerometer measurements synthesized from the Gauss-Markov model of Eq. 10 to evaluate the processor performance. In this application, the processor must be able to design a stable and minimum phase processor constrained so that both resulting poles/zeros lie within the unit circle. These constraints are possible with the subspace **N**umerical algorithm for state-space **S**ubspace **ID**entification (*N4SID*) [19]-[23]. Typically, inverse filter design is a difficult problem; however, with modern subspace identification methodology the *N4SID*-approach is robust enabling a "stable" model to evolve because of the embedded singular value decomposition (*SVD*) numerics employed. With this in mind, we consider 2-input, 3-output, 6-state *MCK*-system depicted in Fig. 1 with transient hammer-strike excitations. Since the *MCK*-system modal frequencies are respectively $f_{modal} = \{0.497, 0.343, 0.123 Hz\}$.

A Gauss-Markov simulation was performed at a sampling frequency of $2Hz$ and process and measurement noise sources with covariances of $R_{ww} = \text{diag}[0.005]$ and $R_{vv} = 0.01$. The synthesized states and noisy *calibration* measurements are shown in Fig. 15 where we observe the 6-states in (a) and accelerometer measurements in (b). In order for the synthesis to be a viable Gaussian simulation the ($Pct.Out/No.$) referring to the percentage and number of samples exceeding the 2σ-bounds should be less than 5%—a 95% confidence interval. For this particular realization at the specified covariances, all of the bounds were satisfied and in fact all were $< 0.5\%$ as shown in the figure.

Using this calibration data and scaled-in-time ($dt = 0.5sec$), hammer-strike excitations, an inverse filter was designed, first using the multichannel state-space algorithm and a 14-state model with the results of the design shown in Fig. 16. Recall that the input sequence to the inverse filter is the calibrated 3-channel measurement with output the 2-channel hammer-strikes. Here we observe the multichannel deconvolution with the extracted excitations shown in (a) and the corresponding estimator statistical tests in (b). Clearly the deconvolved pulse estimates (red) have captured the complete structure of the hammer-strike (turquoise) for each channel confirmed by the zero-mean/whiteness tests (Z-M/W-T) shown in (b). Recall that for optimality, the corresponding residuals must satisfy these criteria over each channel with Z-M:(No. 1–$0.002 < 0.043$), (No. 2–$0.002 < 0.043$) and W-T: (No. 1–$0.44\% < 5\%$), (No. 2–$0.44\% < 5\%$) indicating an optimal design. Next the designed inverse filter was applied directly to synthesized noisy with the results shown in Fig. 17. Here the design is shown in (a) using the *N4SID*-technique to estimate the inverse filter ($\hat{\Sigma}_{inv}$) using the 3-channels of synthesized accelerometer (calibration) data as input and the true mean 2-channel hammer-strikes as the desired signal for the shaping (inverse) filter. The results using a 14-th order state-space processor enabled a 97% fit of the strike data for each channel. Once designed, the inverse filter was applied to noisy data and the results of the multichannel deconvolution are shown in (b) enabling a good extraction of the strike data.

As a final application, a set of independent hammer-strikes we synthesize using the same *MCK*-model and corresponding statistics of the previous excitation; however, now with delays between the independent blows. The simulation was a bit more uncertain with the average percentage of samples lying outside of the 2σ-bounds slightly higher ($< 1.5\%$). The final results of the processor are shown in Fig. 18 with the design in (a) and the application in (b). The design also satisfied the optimality constraints imposed by the zero-mean/whiteness tests (Z-M/W-T) with: Z-M: (No. 1–0.0005 $<$ 0.043), (No. 2–0.0004 $<$ 0.043), (No. 3–0.0002 $<$ 0.043) and W-T: (No. 1–0.88% $<$ 5%), (No. 2–1.74% $<$ 5%), (No. 3–1.03% $<$ 5%) indicating an optimal design.

The results are not quite as impressive as the 2-channel simulation, but still acceptable completing this approach. Perhaps one explanation of these results is that the system is highly coupled and there is channel feedback of the excitations occurring at different times creating more of a disturbance in the coupled channels.

Following the same approach applying the subspace method, the single-channel, Wiener least-squares technique (see Appendix B for details) was applied to the synthesized *MCK*-data of Fig. 15 channel-by-channel designing the inverse filter first followed by its application next. The results of this processor are shown in Fig. 19 with the design in (a) and the application in (b). These results are not as good as the multichannel state-space approach in terms of extracting (deconvolving) the excitation strike shape, but it does adequately capture its structure as shown in the design phase of (a) with application performing reasonably in (b). Here the processor design was based on using all of the samples available from the data (2500-samples) for the final finite impulse response (*FIR*) filter (order).

Finally, along with the hammer-strike all of the excitation signals (DROP, HAZARD, ROAD) were time-scaled and applied as excitations to the *MCK*-system as well. Here the objective was to investigate the performance of the inverse filtering approach as before. The results of each excitation are shown in Fig. 20- 22 with all three excitations specified as *outputs* and the corresponding synthesized response data provided as *inputs* for the inverse filter designs. In all of these scenarios, an optimal design was achieved (Z-M ($<$ .004)) and (W-T ($<$ 2% out)). The DROP excitation design and application results are shown in Fig. 20(a) and (b), respectively. As observed in the figure, the processor is quite capable of extracting the DROP excitation in the design (14-th order,81% fit) comparing the noisy transient excitation (turquoise) with its estimate (red). The application of this filter to noisy data enables a reasonable extraction of the DROP transient impact (red) directly from the synthesized noisy 3-channel data (gray)"true" excitation (turquoise) shown in (b). Similar results extracting the excitations are observed for the HAZARD transient (25-th order, 74% fit) shown in Fig. 21 as well as the ROAD transient (30-th order, 66% fit) shown in Fig. 22—indicating a viable approach to the multichannel problem.

The optimal *SISO* Wiener (channel-by-channel) approach [14] was applied to the HAMMER, DROP, HAZARD, ROAD data sets exciting the *MCK*-system with the results shown in Fig. 23. As expected the designs were quite good indicated in (a) for each of these inputs extracting the excitations with minimal errors; however, the application of the identified

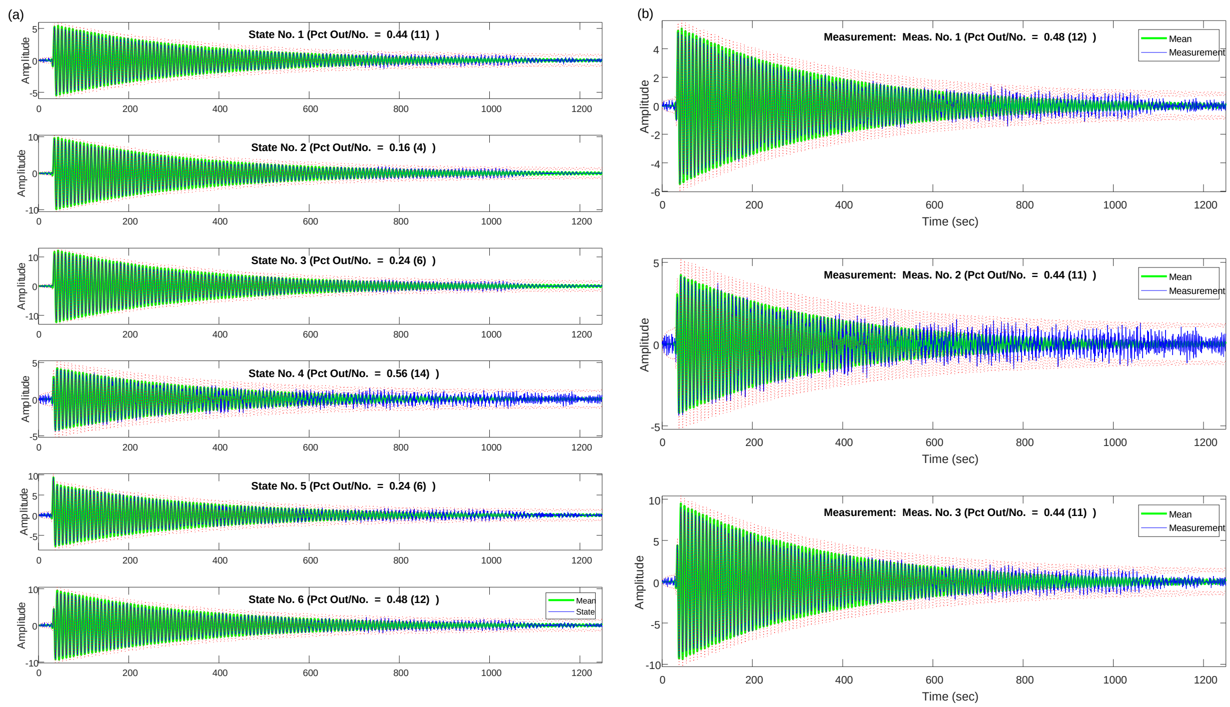

Figure 15: Mechanical System (MCK) a Gauss-Markov Simulation (Noise: $R_{ww} = 0.005$, $R_{vv} = 0.02$): (a) Six (6) modal states: data (blue), mean (green), 2σ-bounds (red dashed)—($Pct.Out < 0.5\%$). (a) Three (3) accelerometer output channels: data (blue), mean (green), 2σ-bounds (red dashed)—($Pct.Out < 0.5\%$).

inverse filter did not perform (see (b)) as well as the multichannel state-space approach possibly because of the internal coupling between modes is not incorporated into a single channel methodology.

This completes the investigation of the inverse filtering approach on synthesized data, next we consider an actual transportation experiment with transient impact excitations.

6 MULTICHANNEL DECONVOLUTION APPLICATIONS

For the deconvolution shock excitations, a simulation capability is under development to synthesize the response of test objects to shock excitations; therefore, a primary objective of this investigation is to identify and extract a variety of shock/vibration signals [18].

Next we develop the processing approach to both enhance the noisy measurements and extract the shock signals of interest. The approach is shown in Fig. 24 where the multichannel measurements are band-pass filtered using a 10^{th}-order Butterworth filter (maximally flat magnitude in the pass band) between the frequency band of $60Hz$ to $4.5KHz$ based

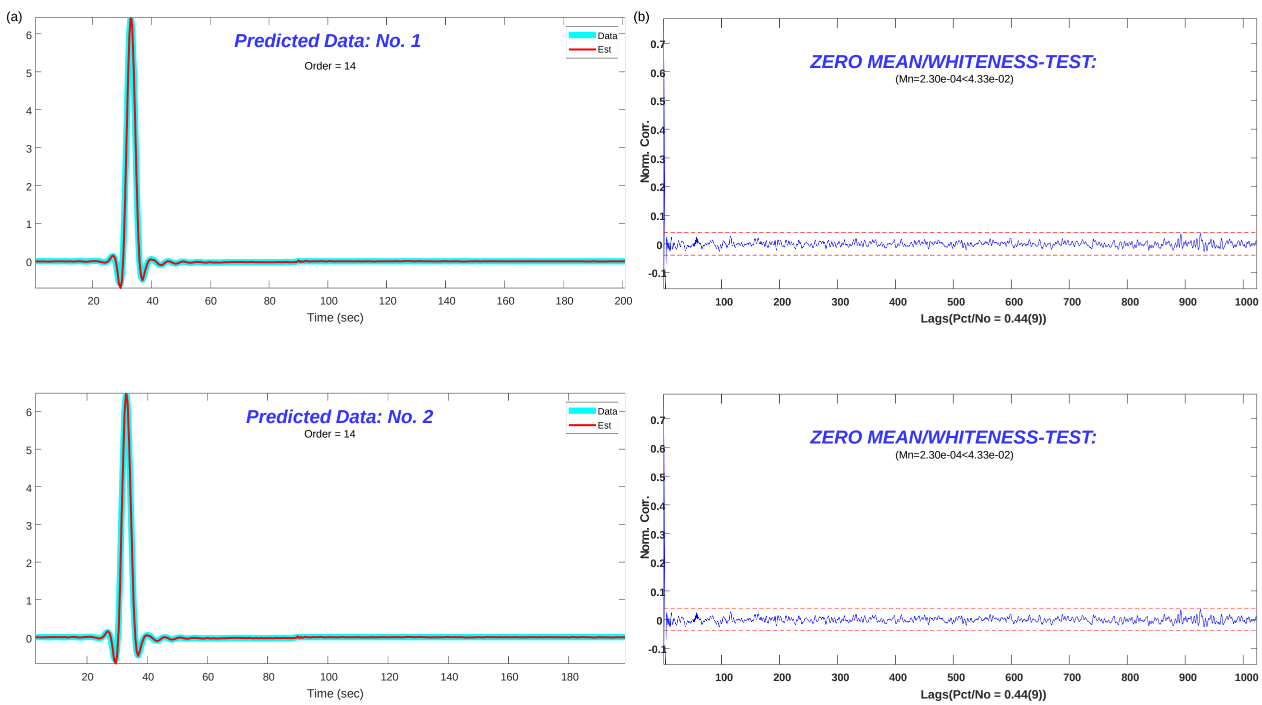

Figure 16: Inverse Filter Design for Excitation Recovery (Deconvolution) of Mechanical System (*MCK*): (a) Hammer-strike (2-channels) recovery estimates (red) synthesized data (turquoise). (b) Performance statistics: Z-M: < 0.043; W-T: $< 5\%$.

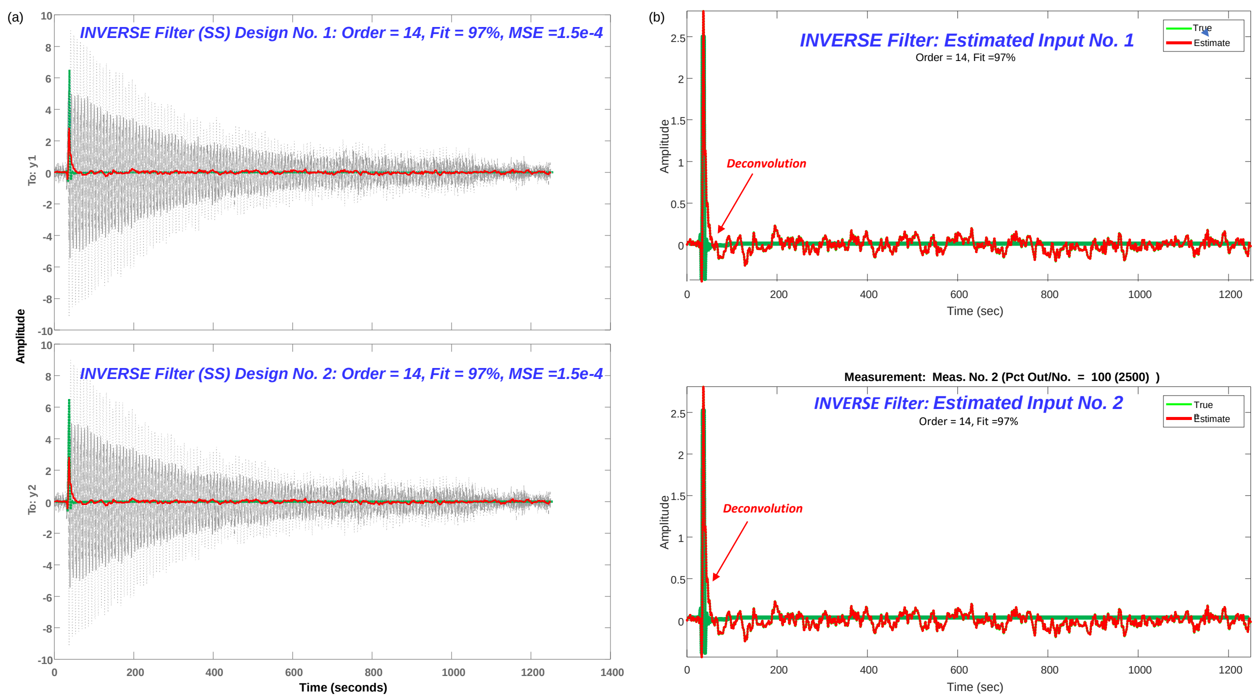

Figure 17: Inverse Filter Subspace Design/Application for Excitation Recovery (Deconvolution) of Mechanical System (*MCK*): (a) *Design:* hammer-strike recovery (2-channel) estimates (red) with true-mean outputs (green) and synthesized accelerometer (3-channels) inputs (gray). (b) *Application:* estimated 2-channel hammer-strike excitations (red) with true mean strikes (green)—InvFilter Order =14 for 97% Fit.

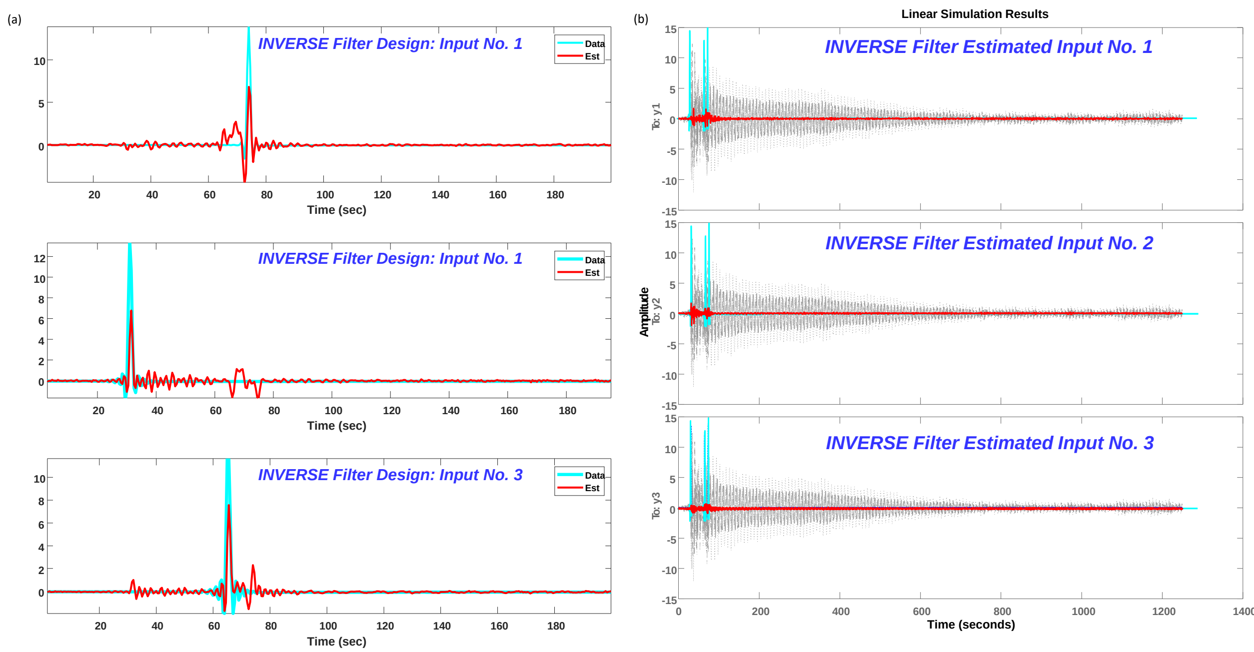

Figure 18: Inverse Filter Subspace Design/Application for Excitation Recovery (Deconvolution) of Mechanical System (*MCK*): (a) *Design:* hammer-strike recovery (3-channel) estimates (red) with true-mean outputs (green) and synthesized accelerometer (3-channels) inputs (gray). (b) *Application:* estimated 3-channel hammer-strike excitations (red) with true mean strikes (green)—InvFilter Order =12 for 36% Fit.

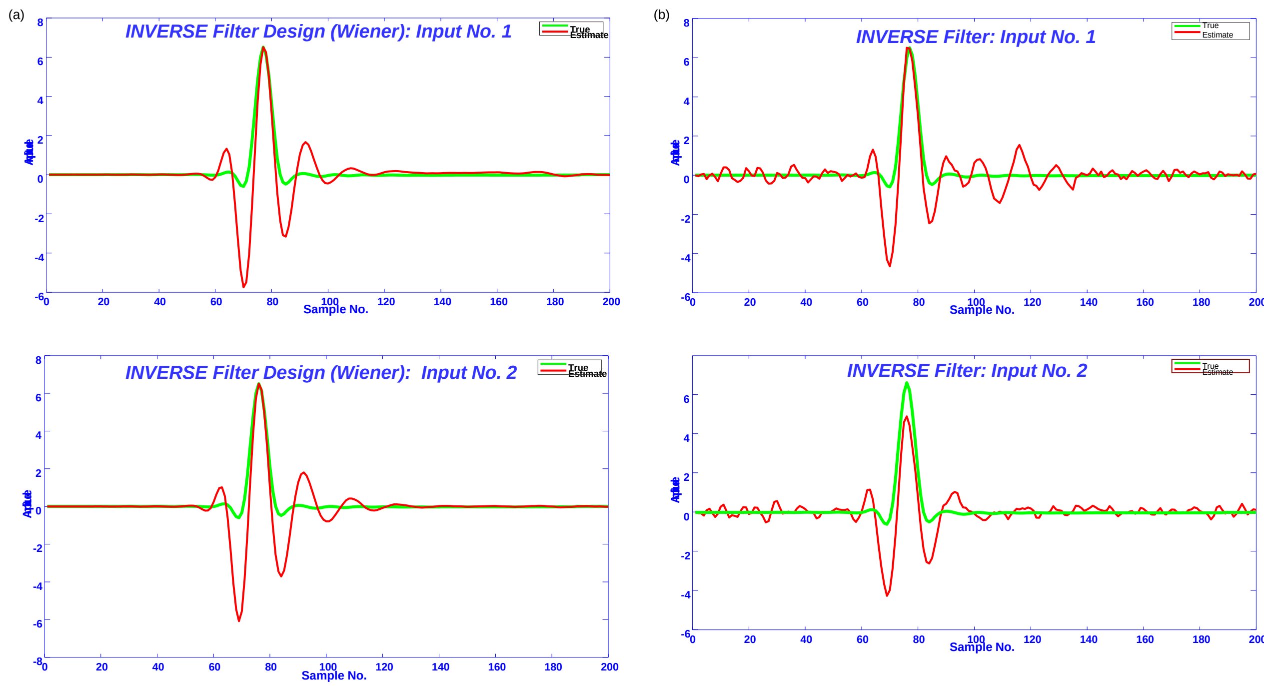

Figure 19: Inverse Filter Wiener Design/Application for Excitation Recovery (Deconvolution) of Mechanical System (*MCK*): (a) *Design:* hammer-strike recovery (single-channel) estimates (red) with true-mean outputs (green). (b) *Application:* estimated (single-channel) hammer-strike excitations (red) with true mean strikes (green)—InvFilter Order =2500.

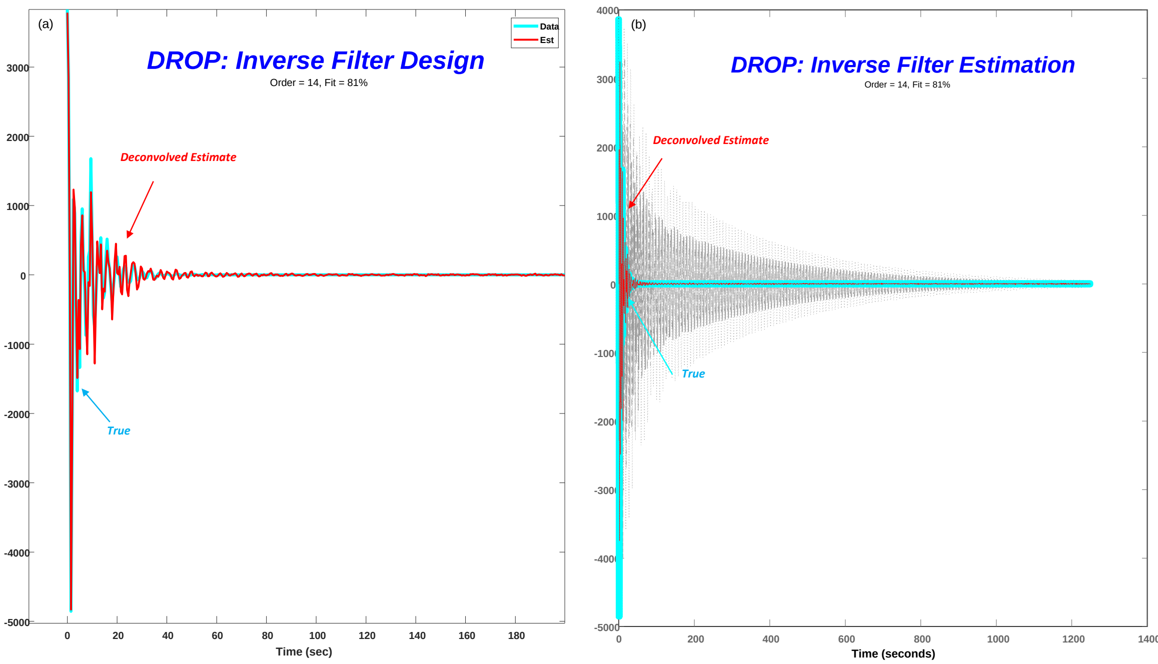

Figure 20: Inverse Filter Subspace Design/Application for Excitation Recovery (Deconvolution) of DROP data: (a) *Design:* DROP recovery (3-channel) estimates (red) with synthesized accelerometer (3-channels) input (turquoise). (b) *Application:* estimated 3-channel DROP excitations (red) with true mean strikes (green)—InvFilter Order =14 for 81% Fit.

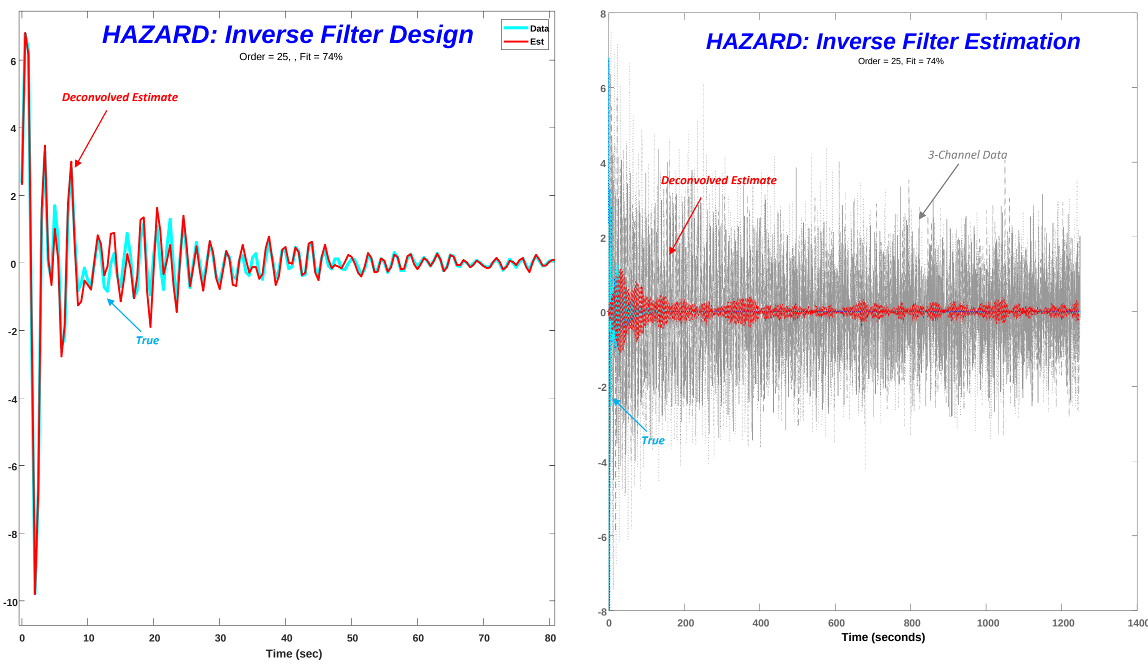

Figure 21: Inverse Filter Subspace Design/Application for Excitation Recovery (Deconvolution) of HAZARD data: (a) *Design:* HAZARD recovery (3-channel) estimates (red) with synthesized accelerometer (3-channels) input (turquoise). (b) *Application:* estimated 3-channel HAZARD excitations (red) with true mean strikes (green)—InvFilter Order =25 for 74% Fit.

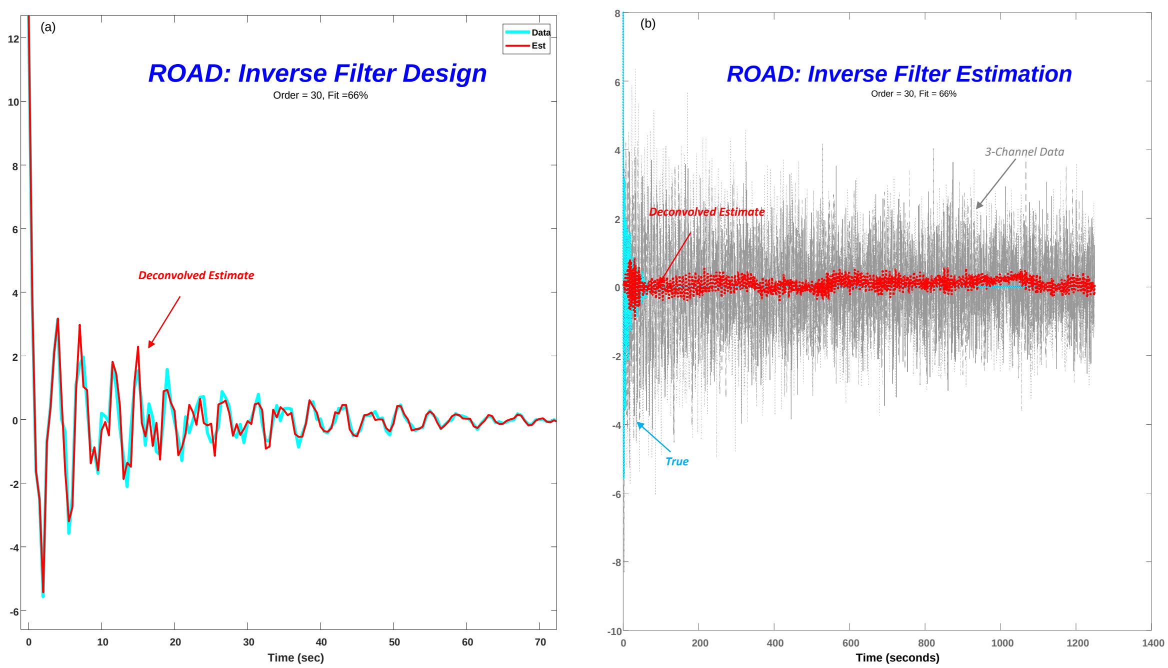

Figure 22: Inverse Filter Subspace Design/Application for Excitation Recovery (Deconvolution) of ROAD data: (a) *Design:* ROAD recovery (3-channel) estimates (red) with synthesized accelerometer (3-channels) input (turquoise). (b) *Application:* estimated 3-channel ROAD excitations (red) with true mean strikes (green)—InvFilter Order =30 for 66% Fit.

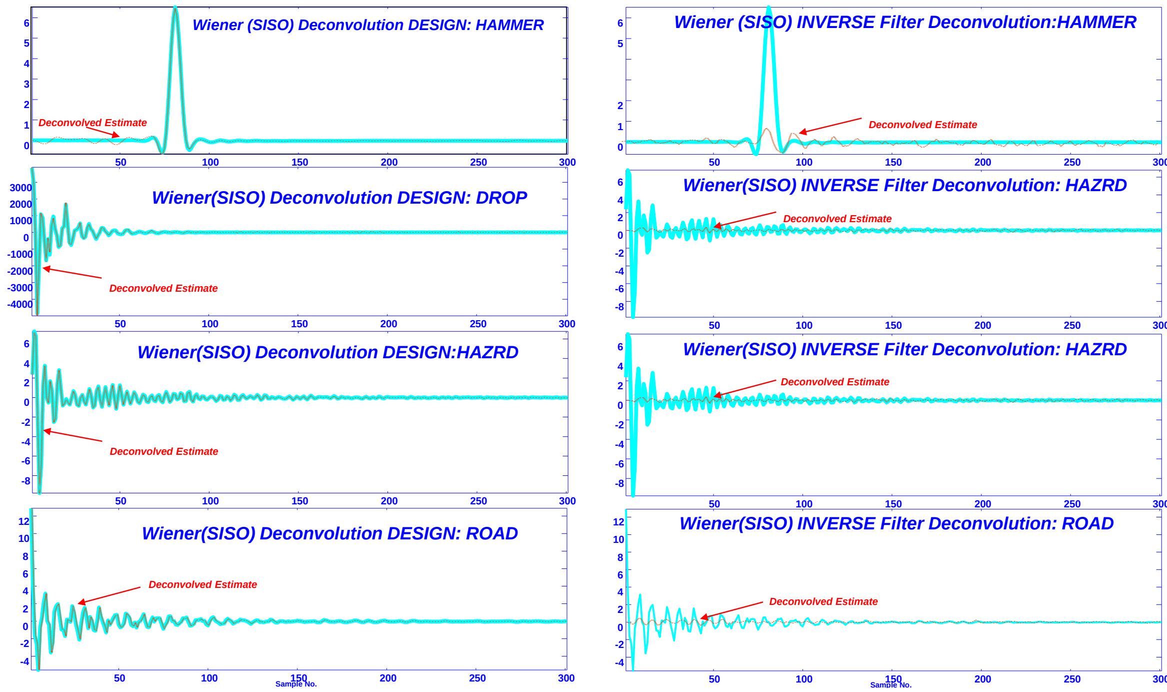

Figure 23: Inverse Filter Wiener Design/Application for Excitation Recovery (Deconvolution) of Mechanical System (*MCK*): (a) *Design:* Recovery (single-channel) estimates (red) with true-mean outputs (turquoise). (b) *Application:* Estimated (single-channel) excitations (red) with true mean (turquoise)—Inverse Filter Order =2500.

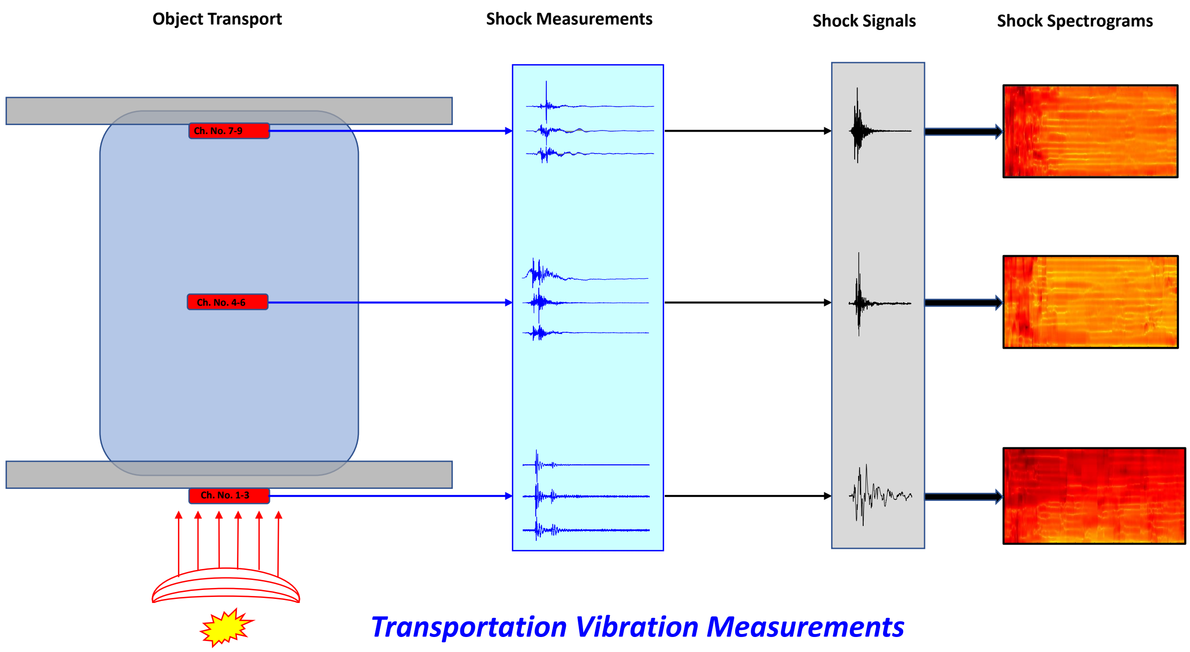

Figure 24: Transportation Vibration Measurements: Test object transport structure with shock excitation, multichannel accelerometer measurements, processed signals and analysis spectrogram.

on the range of expected rigid body modes of the vibrating structure ($< 60Hz$) and the Nyquist frequency of $5KHz$. After examining the resulting spectrum, it was then necessary to equalize or equivalently pre-whiten the data in an attempt to ensure a wide bandwidth for deconvolution of the shock signals. After the equalized array data were available, a multichannel subspace (state-space) impulse response model is extracted and its average signal estimated. The test object channel array data and upper steel plate accelerometer suite data (equalized) were used to perform a multichannel subspace state-space identification (black-box) to obtain impulse response estimates of the system. Once these data are available, the "average" impulse response along with the upper accelerometer measurements are used in an optimal (single channel) deconvolution scheme to extract the shock excitation. Next either the array median or average signal was estimated for analysis and further processing. Here the median processor simply replaces the median value at each time sample (interval) across each the array channel in contrast to an average value, to arrive at the processed signal as illustrated in the figure. Once available, the signal was analyzed with a spectrogram processor producing the frequency-time evolution analysis of the vibration response as well as the deconvolution processor. Based on the approach in Fig. 24, a brief discussion of deconvolution and the subspace identification, spectrogram estimator and deconvolution processor follow.

6.1 Application: Mass-Simulation Transportation Data

A set of transportation data is available from a Mass Simulator—a concrete block. Mass simulator experiments were performed by incorporating a 1500-lb concrete block mounted on a wooden shipping palate—the "Mass Simulator" [18]. The block synthesized a mock test object that was transported in a 48-ft trailer over a typical transportation path in order to acquire shock and vibration excitations. The simulator was mounted over the front axles and instrumented with tri-axial accelerometers located: adjacent to the center-of-gravity (CG) of the block, centered in the trailer bed and above the rear axle. Data were acquired at a $10KHz$ sampling frequency triggered by shock events during the transport. Pre-processed shock time series data for the 9-accelerometer channels are shown in Fig. 26. The raw data were bandpass filtered between, $60 - 4500Hz$ and decimated to a Nyquist frequency of $5KHz$. This data set contains a *high* g-shock event as recorded over the rear axle on channels $4-6$. It is interesting to note that the transient event is weakly recorded over the front axle (channels $7 - 9$) primarily because of the four shock absorbers on both the air-ride trailer and the cab as well as the damping provided by the mass of the block. Channels $1 - 3$ do not indicate the high-g energy of the event, since it was hardware constrained by a low-pass filter ($450Hz$). The shock, itself, was produced (unintentionally) by the trailer riding over a large road surface separation at different levels causing a g-force event as shown by the large transient recorded on the Z-direction channel (No. 6) and indicated on the X, Y-channels (No. 4 and 5) as well. This shock event is assumed to represents a "pure" input excitation that might be expected during transport.

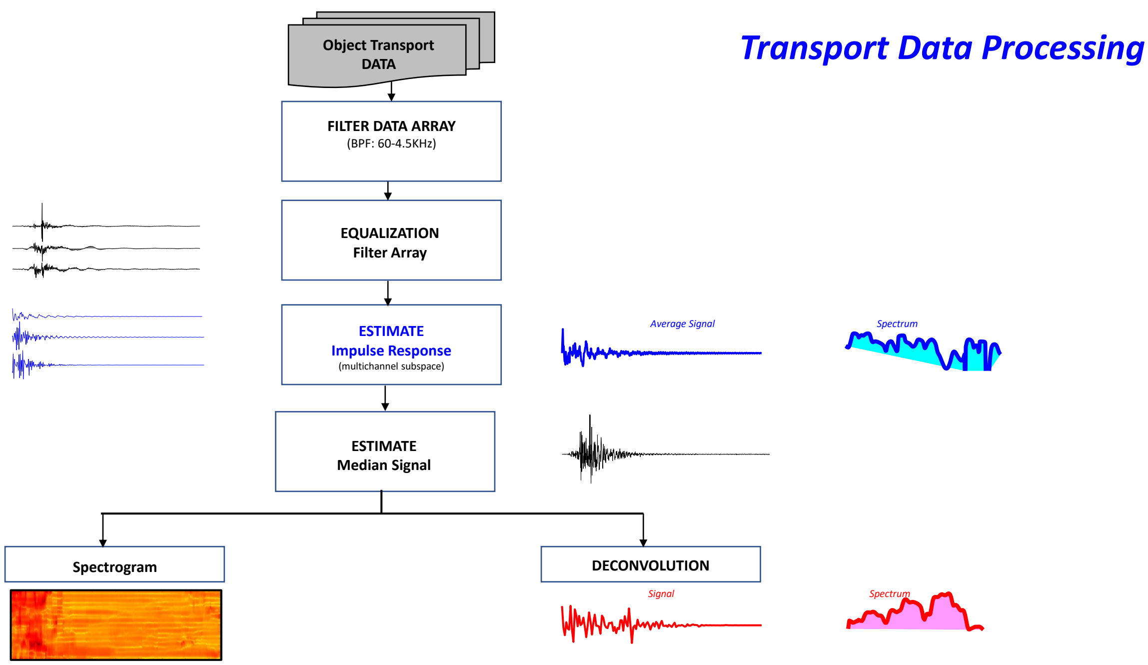

Figure 25: Transportation Data Processing: Array multichannel bandpass filtering ($60 - 4500\ Hz$), multichannel equalization filtering (1^{st}-order), multichannel subspace impulse response identification, array median signals for spectrogram analysis and deconvolution processing.

The data were further processed extracting the primary shock event (*high g*-shock) and analyzed extracting the "pure" sequence and its largest shock transient. After decimation and trend removal, the data were equalized (whitened) for analysis. These channel shock measurements and their corresponding spectra were estimated with the results shown in Fig. 27. The X, Y, Z-channel data clearly shows a consistent structure in (a) with the corresponding ensemble spectra shown in (b). The spectral bands of this shock excitation are centered at the following frequencies (bandwidth): $200Hz(BW : 150)$, $450Hz(BW : 150)$, $650Hz(BW : 100)$, $850Hz(BW : 225)$, $1250Hz(BW : 250)$, $1550Hz(BW : 150)$, $1850Hz(BW : 200)$ and $2050Hz(BW : 125)$. The *median* shock signal was estimated with its corresponding spectrogram shown in Fig. 28. From the figure, the instantaneous ensemble spectra (green) indicates a multitude of spectral resonances stretching across the bands as confirmed by its corresponding peak histogram below in red.

Multichannel spectral estimation was performed using a 40-th order state-space method (N4SID) with the results shown in Fig. 29 where the "fit" is compared to the median estimates of the data (blue) and equalized data (green) as well as the extracted shock pulse event (red). It is clear that the estimator has captured the salient spectra coupled directly to this event. The resonant bands (turquoise filled) clearly illustrate the excitation bands.

The excitation and accelerometer data were pre-processed (filtered, decimated, trend removed, normalized) as shown in Fig. 30(a) where a set of extracted shock excitation transients and their corresponding ensemble spectra are given along with the subsequent response data and spectra in (b). Multichannel deconvolution (design) was performed by estimating (N4SID) an inverse filter using a 40-th order state-space model applying the excitation data as the *output* and the response data as the *input* [14], [19].

The results of the inverse filter design are shown in Fig. 31 where the true excitation data (turquoise) and their estimates (red) are overlayed in (a). Recall that the Z-M test requires that the estimate should lie below the bound (0.17) , while the W-T insists that 95% of each channel correlation estimates lie within the bounds or equivalently 5% are outside. For the design, the Z-M/W-T results for each measurement are: (No. 1: 0.022/6.3%), (No. 2: 0.058/6.3%), (No. 3: 0.026/4.7%).

The application of the inverse filter processor to measurement data is shown in Fig. 32 where the average data spectrum is compared to the average deconvolved spectrum. The results are encouraging, since the spectral bands of high interest are capture by the processor.

6.2 Application: Vibrating Structural Test Object Data

In this section, we discuss the application of the multichannel deconvolution approach to a structurally "unknown" structural object, that is, a complex, stationary structure (black-box) with no rotating parts that is subjected to random excitations with accelerometer sensors placed on its surface and around its periphery. Here the primary objective of this controlled experiment is to examine the feasibility of applying the model-based deconvolution technique to a mulitple input/multiple (*MIMO*) structural system subjected to environmen-

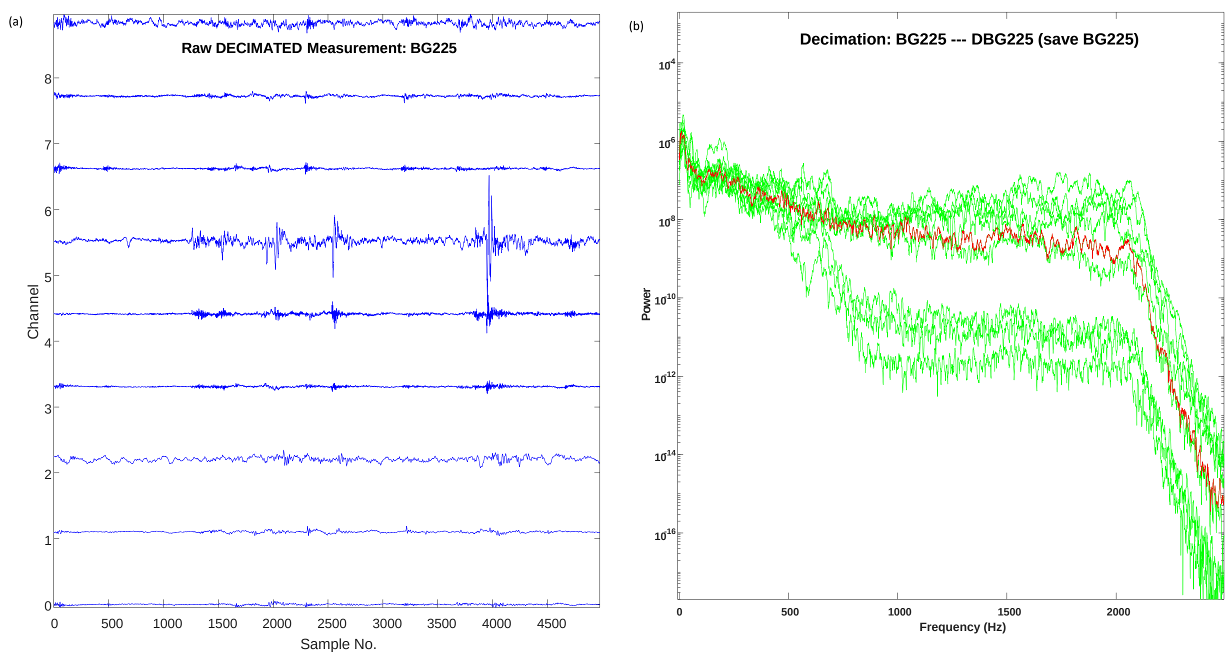

Figure 26: Mass Simulator Transportation Data: (a) Tri-axial accelerometer channel time series. (b) Ensemble power spectra (green) and mean (red).

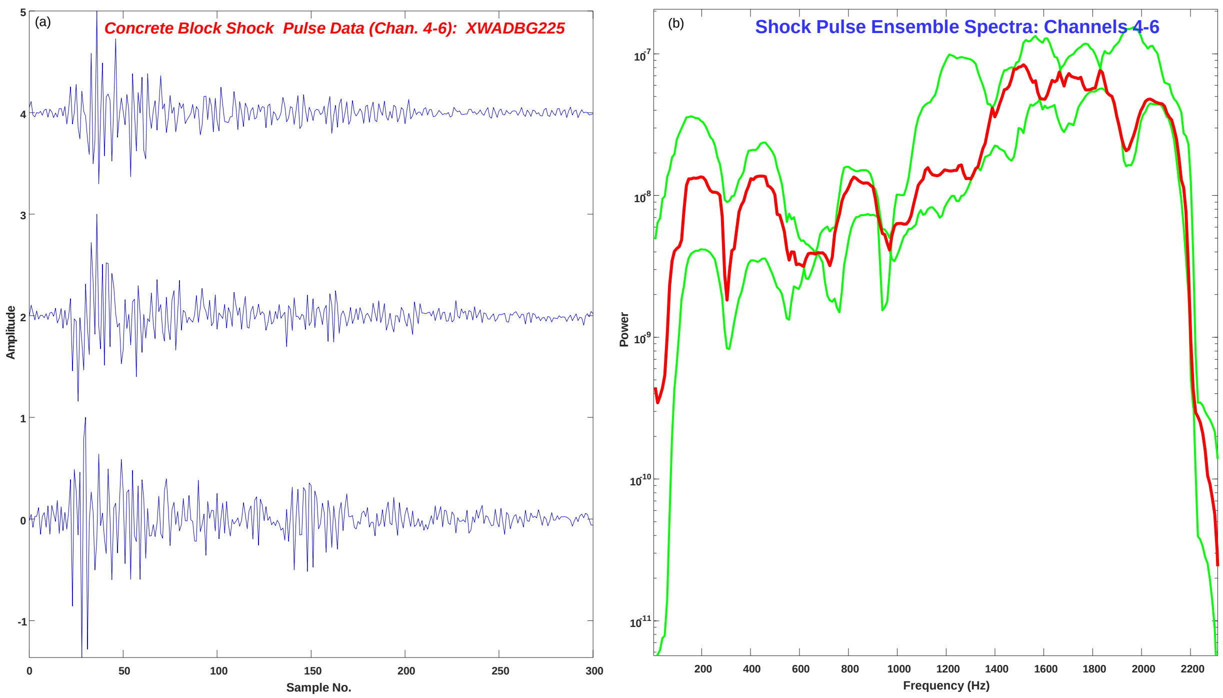

Figure 27: Mass Simulator Transportation Data (Chan. $4-6$): (a) Tri-axial accelerometer channel time series (Shock Pulse (XYZ)). (b) Ensemble power spectra (green) and mean (red).

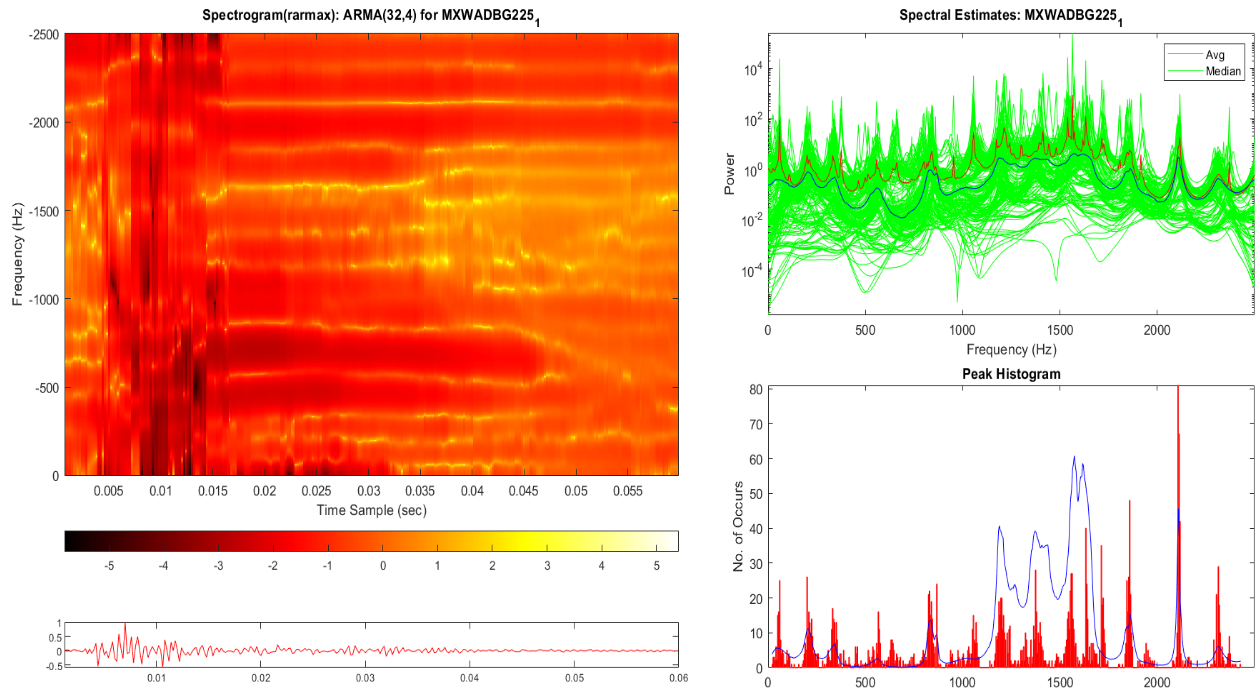

Figure 28: Mass Simulator Transportation Data (Chan. $4-6$) Spectrogram: spectrogram, signal (red), ensemble power spectra (green) and mean (red) and peak histogram (red).

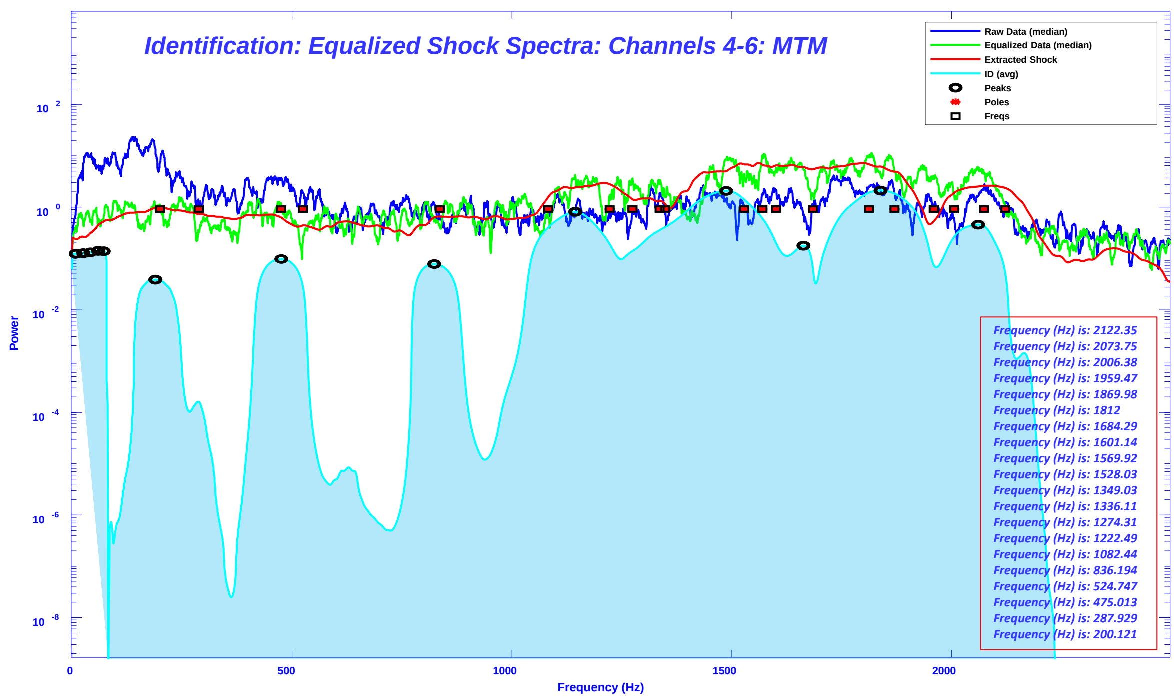

Figure 29: Multichannel Spectral Estimation of Mass Simulator Transportation Data (Chan. $4-6$): Raw data (median), pre-processed median data (trend removed) (green), extracted (equalized) shock pulse event (red) and average identified spectrum (turquoise filled).

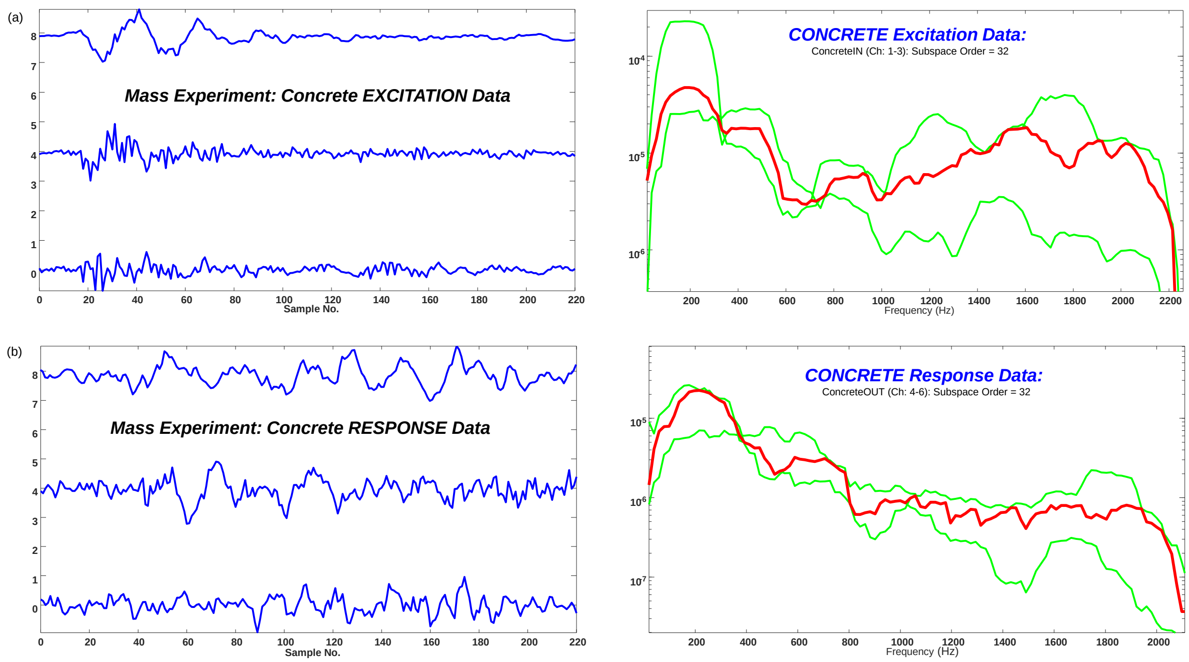

Figure 30: Mass Simulation Experiment Data: (a) Multichannel excitation (input) data and ensemble (green) with average (red) spectra. (b) Multichannel response (output) data and ensemble (green) with average (red) spectra.

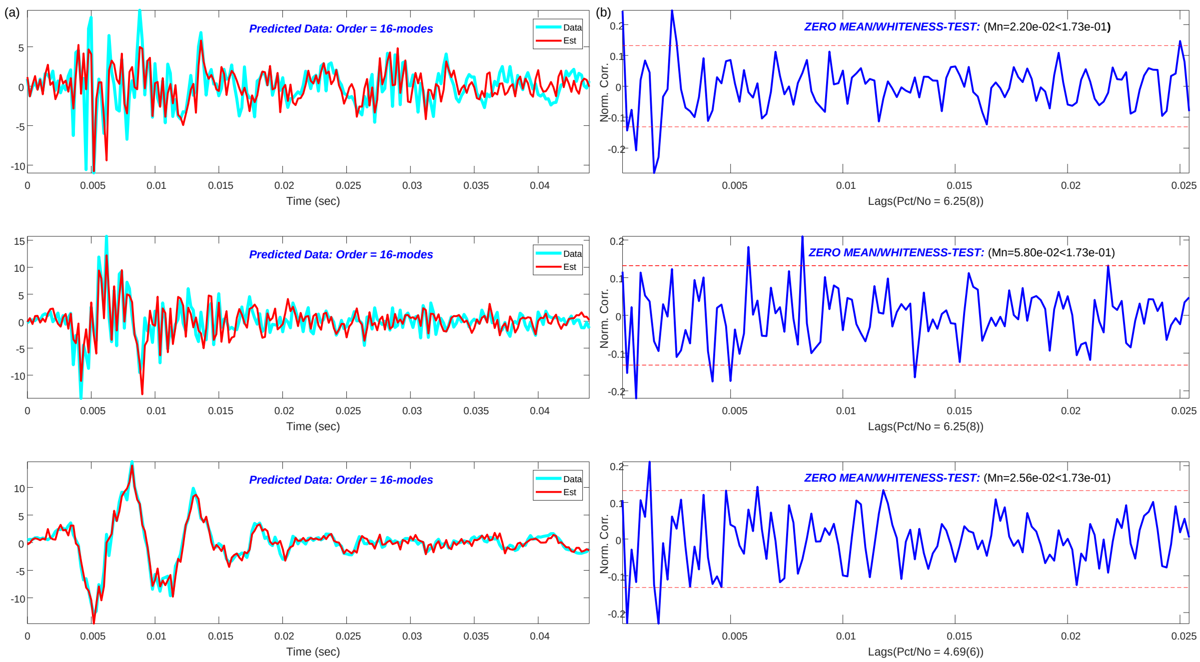

Figure 31: Mass Simulation Experiment: Inverse Filter Design for Excitation Recovery (Deconvolution). (a) *Design:* Recovery (multichannel) subspace (order = 16-modes) estimates (red) with true-mean outputs (turquoise). (b) *Performance:* Zero-Mean/Whiteness optimality tests: Z-M/W-T are: (No. 1: 0.022/6.3%), (No. 2: 0.058/6.3%), (No. 3: 0.026/4.7%).

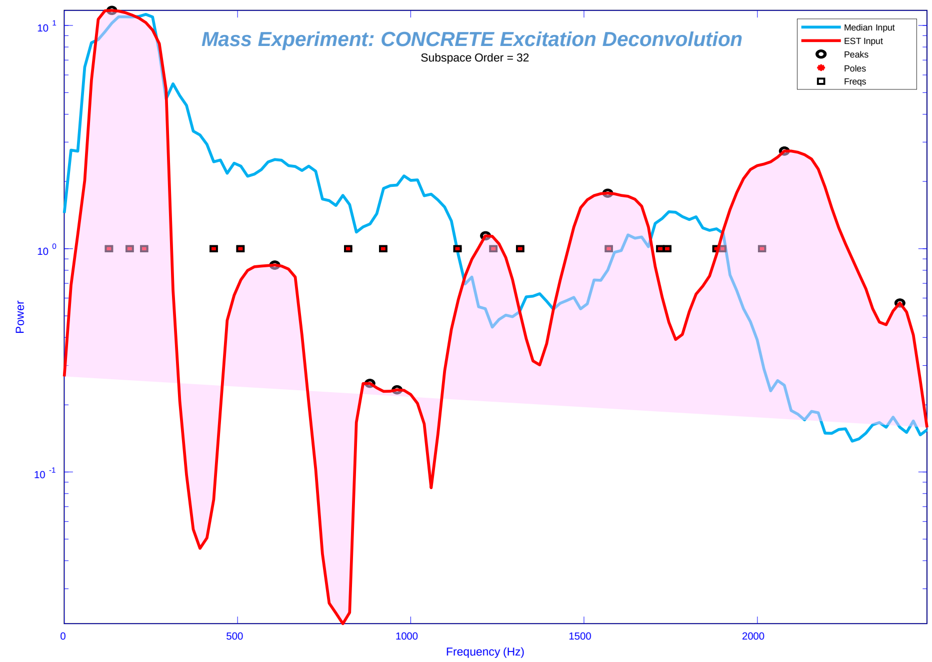

Figure 32: Mass Simulation Experiment Inverse Filter Design Spectra: Average excitation (turquoise) spectrum and average recovered (deconvolved) excitation (red filled) spectral estimate.

tal disturbances and noise. However, we do have some prior information about its test object modal response from historical tables and use this information as a guiding principle to pre-process the acquired data. The structural object under test was subjected to random excitations by placing a stinger or motor-driven rod perpendicular to the base of the structure as illustrated in Fig. 33. A suite of 19-triaxial accelerometers were positioned strategically about the structural object surface as well as a single triaxial (XYZ) sensor allocated to measure the excitation time series. In total, an array of 57-accelerometer channels acquired a set of 10-minute duration data at a $6.4KHz$ sampling frequency [24], [25]. For pre-processing the data were subsequently down-sampled to $2.5KHz$ in order to focus on the range of the excitation frequencies ($< 1.25KHz$). For this investigation, a subset of the 8-triaxial accelerometers was selected as well as the single triaxial sensor on the output excitation of the stinger. Therefore, from the state-space perspective our *MIMO*-system, is a targeted system of up to a maximum of 12-modes or 24-states with an array of 24-channels (XYZ) of time series measurements and 3-channels (XYZ) of an excitation measurement that we are attempting to recover from these noisy accelerometer measurements using an inverse filter.

The raw (down-sampled) data represent the expected data windows (5000 samples) acquired from a real-time acquisition system. The windowed responses (time series) were pre-processed, that is, they were outlier corrected, equalized (whitening filter), bandpass filtered ($150 - 1.1KHz$), and normalized (mean removal/unit variance) prior to performing the inverse filter design. Once pre-processed the input/output data with roles reversed were provided to the subspace algorithm enabling an identification of a stability constrained, state-space model of the inverse filter, $\Sigma_{INV} = \{A_{INV}, B_{INV}, C_{INV}, D_{INV}\}$. With the design accomplished, the inverse filter was applied to an independent section (5000 samples) of noisy accelerometer data to validate multichannel deconvolution processor performance.

The *MIMO*-data of the controlled experiment are shown in Fig. 34 where the triaxial (XYZ) random excitations with their accompanying ensemble spectra are shown along with the 8-triaxial accelerometer responses (24-channels) on the surface and periphery of the structural object and ensemble spectra. The question to be answered is whether or not the multichannel deconvolution technique using an inverse filter is capable for extracting these excitations from the noisy accelerometer array data. We investigate this problem in two-phases: XYZ-data sets individually (8 directional outputs and 1-input) and the combined measurement array directly (24-outputs and 3-excitations). The simpler XYZ-data sets are investigated first followed by the combination or batch data.

The design procedure is to: (1) *Calibration*: design the *MIMO*-inverse filter using the state-space subspace identification method constrained for stable solutions only; (2) *Application*: process the incoming accelerometer measurements with $\Sigma_{INV}$to extract the excitations. The performance metrics that can be used are: the percentage of model fit (Fit %) to the data and its corresponding mean-squared error (*MSE*). This procedure is applied, starting with the individual XYZ-directional data sets where the results for the X-channel data is shown in Fig. 35(a) where the estimated excitation (red dots) is overlaid on the actual

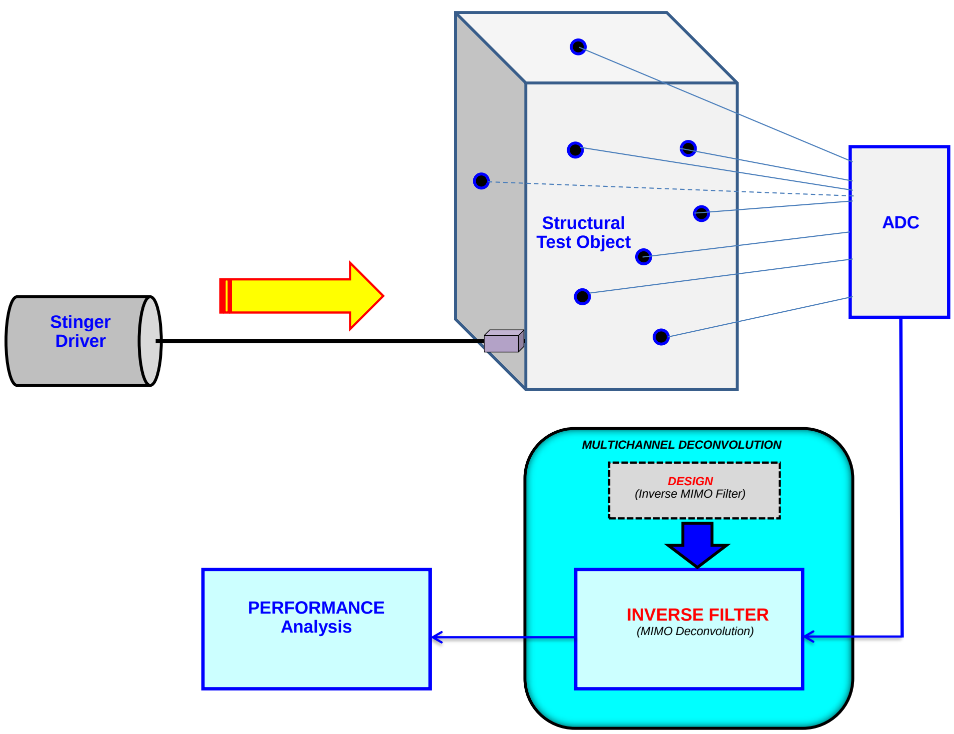

Figure 33: Structural Test Object Experimental Setup: Motor driven stinger (random excitations), accelerometer sensor measurements, *MIMO* analog-to-digital (A/D) acquisition, inverse filter (DESIGN), multichannel deconvolution, (INVERSE FILTERING), performance analysis.

(initial) excitation (turquoise) with the subspace "fit" using a 25-mode model to the data is at 44.4% and the *MSE* at 0.29. The optimality tests (zero-mean/white) indicate an optimal subspace design as Z-M/W-T: 0.009/4.9%. Note that since the excitations are random signals, then a reasonable comparison is the power spectra as shown in (c). It is clear that the design spectrum (red-filled) has captured the prominent spectral characteristics of the original excitation. The application of the inverse filter to another section of noisy measurement data (8-channels) also demonstrates the robustness of this approach, since the extracted excitation spectrum (green) also captures the salient features of the original excitation data (turquoise). The resonant peaks (red list) and the identified modal peaks (red squares) are also shown overlaid on the spectral plots.

The multichannel deconvolution results for the Y-channel data shown in Fig. 36. Again the estimated excitation (red dots) is overlaid on the actual (initial) excitation (turquoise) where the subspace "fit" using a 25-mode model to the data is at 55.8% and the *MSE* 0.17—somewhat better than that of the X-channel. The optimality tests (zero-mean/white) indicate an optimal subspace design as Z-M/W-T: 0.006/4.7% with slightly better statistics as well.

Finally for the individual directional data, the multichannel deconvolution of the Z-channel data is depicted in Fig. 37 as above. The results are better than those of the previous individual channel data primarily because of a higher directional sensitivity (better *SNR*) to the induced vibrations. In this case, the the subspace "fit" again using a 25-mode model to the data is at 66.0% (best) and the smallest *MSE* of 0.11—somewhat better than that of the other channels. The optimality tests (zero-mean/white) indicate an optimal subspace design as Z-M/W-T: 0.003/6.6% (slightly larger %).

Next we consider the "batch" of all of the sensors combined as a *MIMO*-system of 3-excitations (inputs) and 24-responses (outputs) of Fig. 34. The inverse filter design results as a *MIMO*-system is shown in Fig. 38 where the overlaid fits and Z-M/W-T are shown. Here the subspace "fits" using a 20-mode model to the excitation data are at (35%,33%,31%) and the respective *MSE* at 1.25 not as good as the individual XYZ-channel results. The optimality tests (zero-mean/white) were also not quite as good for an optimal subspace design as Z-M/W-T: (0.005/7.6%; 0.003/8.3%; 0.005/7.7%). This could be because a lower *SNR* for the combination of batch channels as well as the fact that individual deconvolvers were design directly from each excitation separately. Next the inverse filter was applied directly to the 24-channel response data with the results shown in Fig. 39 depicting the deconvolution of each of the raw excitation channels (dotted blue,green,red). The similarity of the channel excitation spectra (solid blue,green,red) is quite good and clearly captures the major frequencies (list) available from the subspace identification.

This completes the discussion of the results of applying the *MIMO* deconvolution technique using the multichannel inverse filter subspace design as compare to the individual channel designs. Even though the individual designs indicate a slightly superior performance, the batch design option may prove to be quite adequate in some applications. Thus, both methods provide reasonable solutions to the multichannel deconvolution problem on

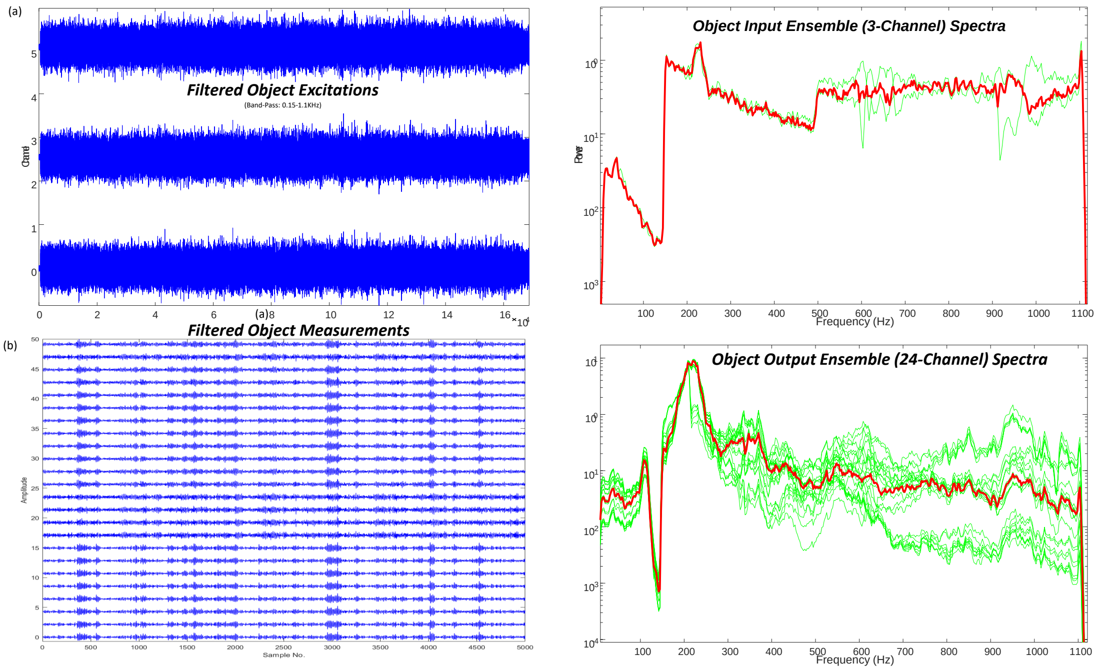

Figure 34: Test Object Data: (a) Multichannel (3-channels) random excitation (input) data and ensemble (green) with average (red) spectra. (b) Multichannel (24-channels) response (output) data and ensemble (green) with average (red) spectra.

real data.

7 Summary

Transporting critical structural objects of high interest is a viable problem from the initial shipping/packaging and subsequent vibrational response inflicted during actual transport by rail, highway, sea or air. This leads to the need to extract any of the potential excitation incurred in order to assess the potential damage an assess subsequent structural failure leading to a deconvolution problem from the signal processing perspective. The multichannel or multiple input/multiple output (*MIMO*) deconvolution problem for transporting critical test objects is investigated here by developing a shaping or inverse filter design based on a state-space (subspace) identification technique. The inverse filter is designed during calibration tests and applied to noisy multichannel accelerometer measurement data demonstrating a reliable and timely approach to solving this critical problem.

The overall object of this effort is to extract and analyze the corresponding input (shock) excitations that could be incorporated into an Impulse-Event simulation model under development [17]. In order to achieve the objective, input excitation extraction, a multichannel identification method (*N4SID*) is briefly discussed along with a recursive-in-time spectro-

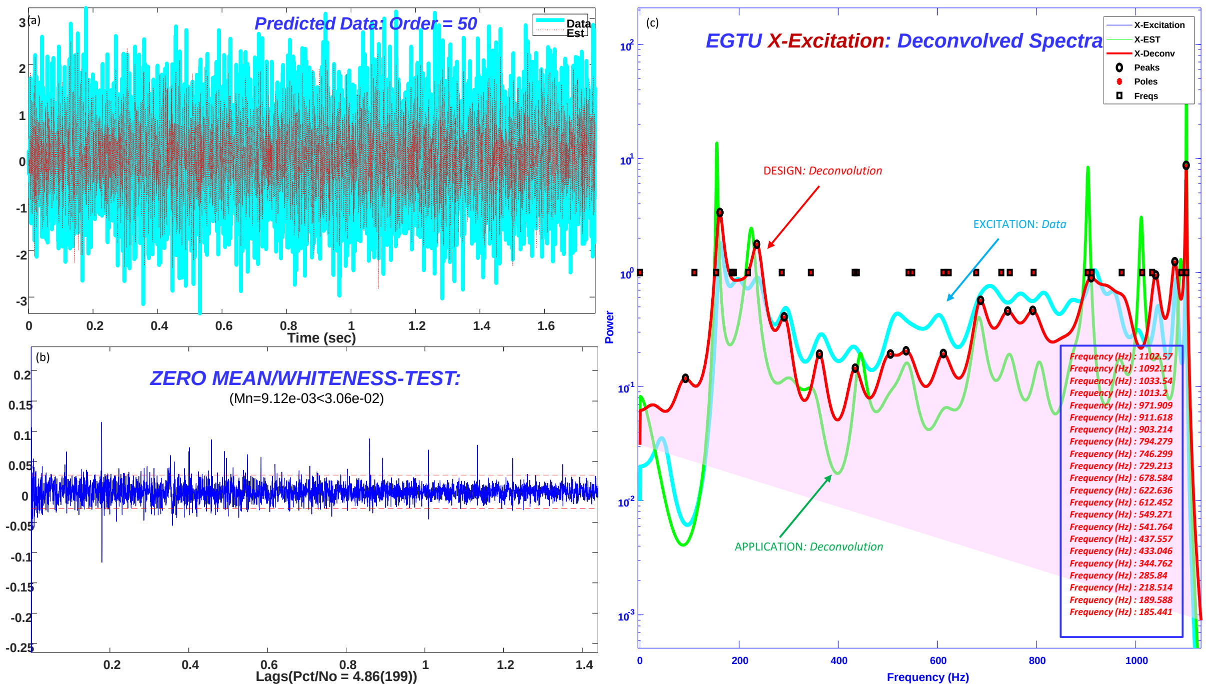

Figure 35: Test Object X-Channel Data (8-Measurements,1-Excitation): (a) *Design:* Recovery (multichannel) subspace estimates (Order = 25-modes, Fit = 44.4%, MSE = 0.29). (b) *Performance:* Zero-Mean/Whiteness optimality tests: Z-M/W-T are: (No. 1: 0.009/4.9%). (c) Deconvolution spectra: Excitation (turquoise), inverse filtered application (green) and design deconvolution (red) including peak frequency estimates (list).

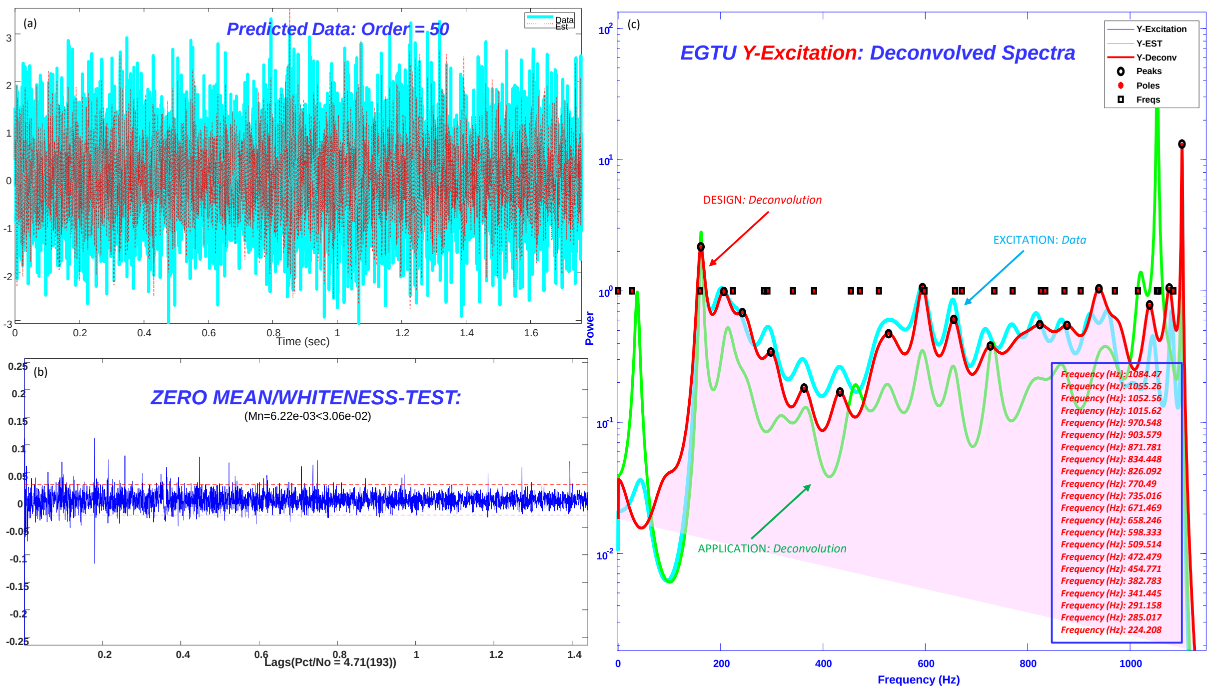

Figure 36: Test Object Y-Channel Data (8-Measurements,1-Excitation): (a) *Design:* Recovery (multichannel) subspace estimates (Order = 25-modes, Fit = 55.8%, MSE = 0.17). (b) *Performance:* Zero-Mean/Whiteness optimality tests: Z-M/W-T are: (No. 1: 0.006/4.7%). (c) Deconvolution spectra: Excitation (turquoise), inverse filtered application (green) and design deconvolution (red) including peak frequency estimates (list).

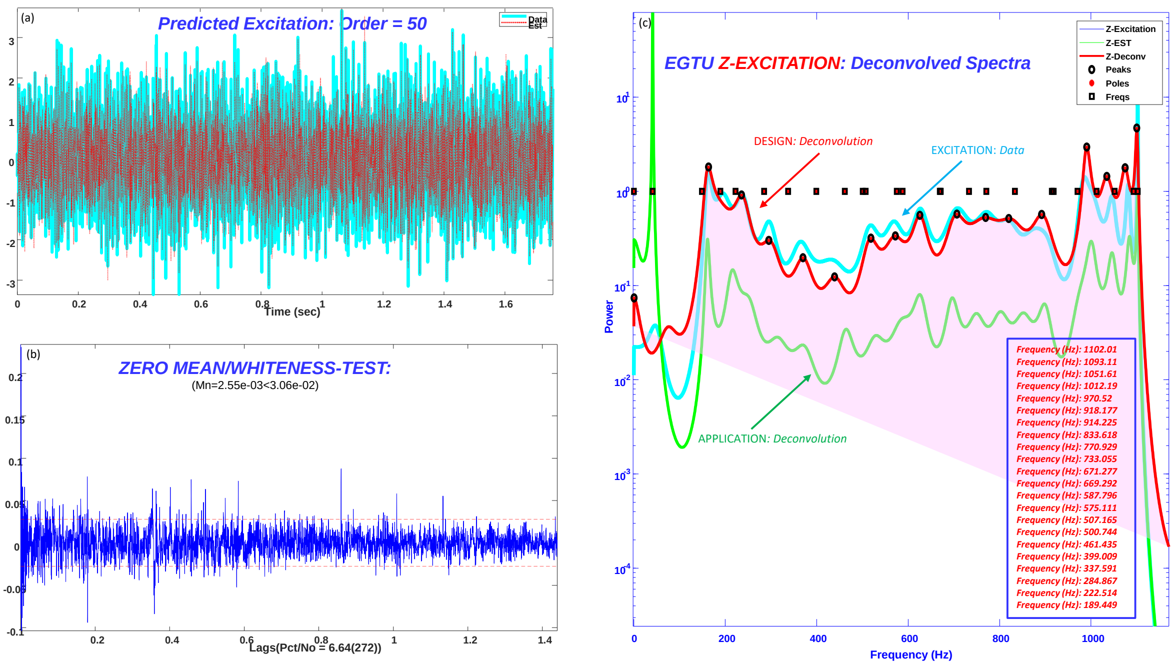

Figure 37: Test Object Z-Channel Data (8-Measurements,1-Excitation): (a) *Design:* Recovery (multichannel) subspace estimates (Order = 25-modes, Fit = 66.0%, MSE = 0.11). (b) *Performance:* Zero-Mean/Whiteness optimality tests: Z-M/W-T are: (No. 1: 0.003/6.6%). (c) Deconvolution spectra: Excitation (turquoise), inverse filtered application (green) and design deconvolution (red) including peak frequency estimates (list).

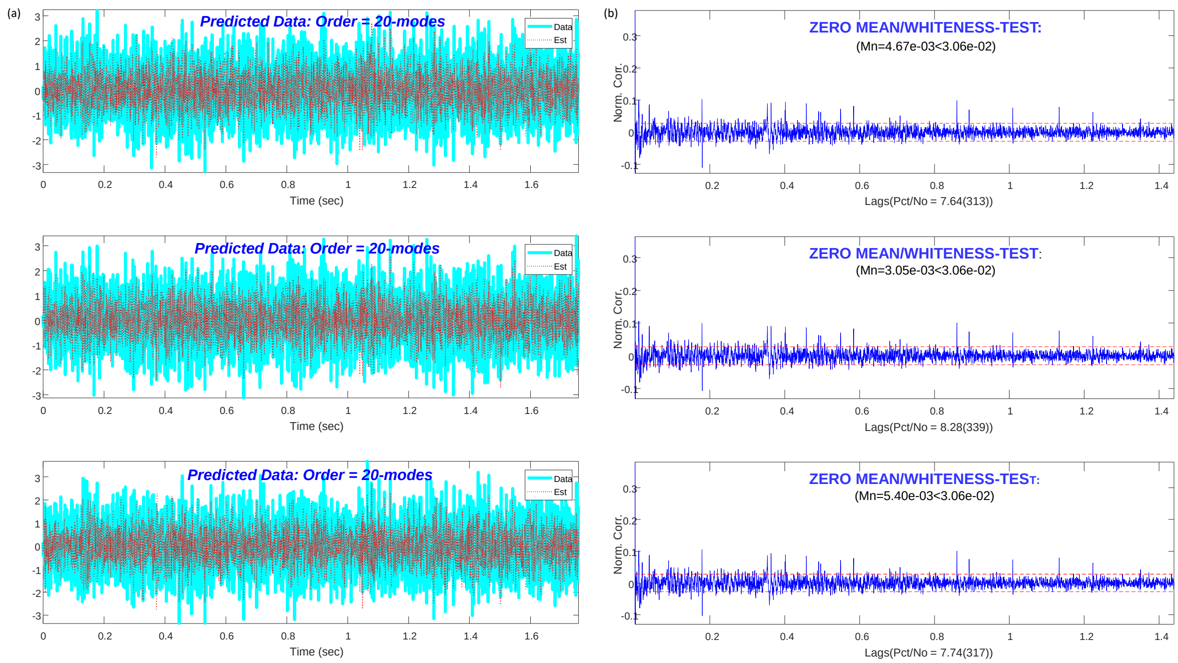

Figure 38: Test Object DESIGN: Inverse Filter Design (3-Channels) for Excitation Recovery (Deconvolution). (a) *Design:* Recovery (multichannel) subspace (Order = 20-modes, Fits = 35%,33%,31%) estimates (blue,red,green) with corresponding raw excitation data to match (blue,red,green)) and *Performance:* Zero-Mean/Whiteness optimality tests: Z-M/W-T are: (No. 1: 0.005/7.6%), (No. 2: 0.003/8.3%), (No. 3: 0.005/7.7%).

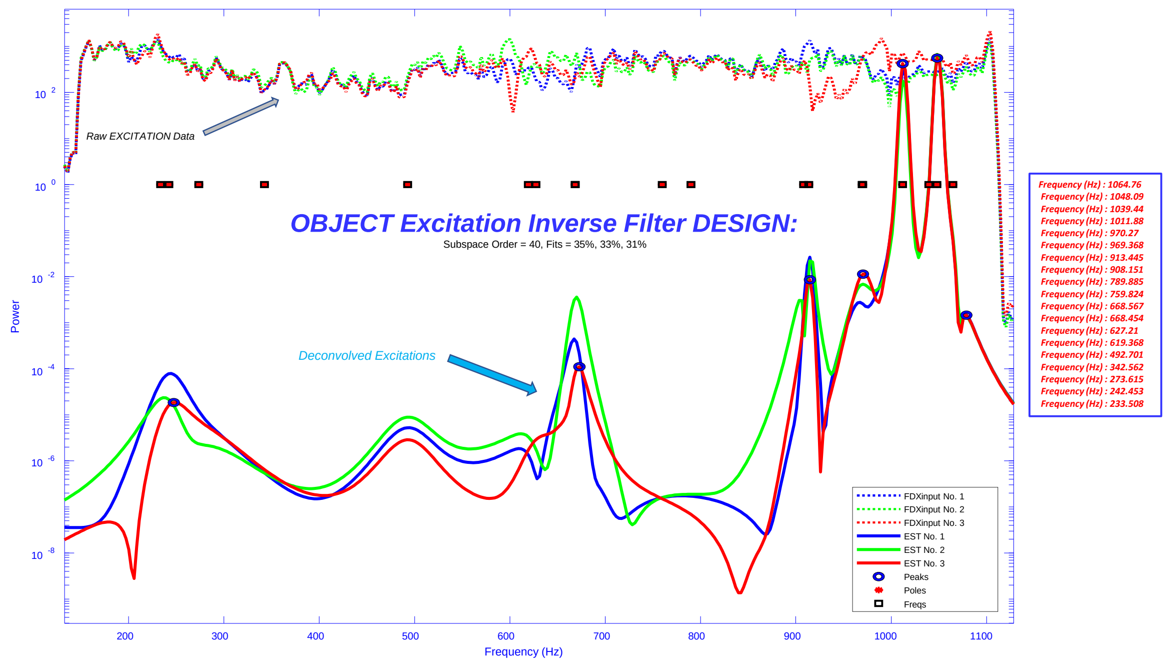

Figure 39: Test Object Inverse Filter Design Spectra: Raw excitation (blue,red,green-dotted) spectra (3-Channels) and recovered (deconvolved) excitation (blue,green,red) spectral estimates including peak frequency estimates (list).

gram estimator and single channel deconvolver using a so-called Wiener mean-squared error technique [14].

After discussing the classical multichannel representation of a vibrating structure and its accompanying state-space characterization, the Impact Problem is introduced along with a set of potential excitation signals gathered from a variety of shipments. A canonical 3-mode,$1-3$-excitation problem was developed to illustrate the approach and provide a quantitative measure to evaluate its deconvolution performance. It is shown that indeed the inverse filter design and application is capable of performing quite well on synthesized data ranging from HAMMER strike transients and actual shipping roadway excitations: DROP, HAZARD and ROAD.

Next a Mass Simulation Experiment was performed employing a large concrete block as the synthesized test object that was packaged and shipped in an instrumented tractor/trailer vehicle along typical roadways to obtain both excitation and response signals for analysis and performance evaluations. The basic idea is to extract shock and vibration excitation signals that test objects experience during a typical transport scenario. During test object transport "known" shocks (drops) occur and are processed along with minor shocks during various segments of travel yielding valuable data sets. The results are again quite good enabling a successful extraction of the excitation inputs.

Finally, the vibrational response of an actual structural test object was investigated with recorded random excitation inputs from a shaker test. Again the results are quite encouraging indicating that the shaping or inverse filter design and application provide a meaningful methodology that can be applied to extract random transient excitations during transport of critical structural test objects to assess potential damage and ensure reliable operation.

This method of "transport" testing has added-value providing yet another capability beyond simulation, shaker and laboratory tests. This approach can be used to validate processing methods and custom electronics designed to solve the Impact-Event or Drop Problem monitoring, detecting and localizing potential structural test object failure mechanisms.

8 Acknowledgments

This work performed under the auspices of the U.S. Department of Energy by Lawrence Livermore National Laboratory under Contract DE-AC52-07NA27344. The authors would like to recognize Mr. H. Teng and Mr. S. Franco for providing the data sets for the mass simulation and test object shaker data along with Mr. J. Case, B. Illingworth and J. Cook for helpful discussion on the problem throughout this effort.

APPENDIX A: Subspace Impulse Response Estimation

The development of multiple input/multiple output subspace techniques are investigated to identify or extract the "black-box" multichannel impulse response of the overall acoustic system from noisy vibrational measurements. The advantage of this multichannel identifier is that it incorporates all of the mutual/cross coupling information into the processor providing a reasonable "fit" enabling an excellent extraction of the resonant frequencies (see Refr. [19]-[23] for more details). Such a representation provides us with a reasonably accurate response required to perform the deconvolution of the shock excitation—the primary purpose of this effort.

The main objective of subspace techniques is to extract an extended observability matrix directly from the acquired data first, followed by the state-space, system model second. The underlying mathematical foundation that enables these extractions is projection theory. The primary idea, when applied to this problem, is to perform projections in a Hilbert space occupied by random vectors. That is, if $\mathbf{y}_f(t)$ is a random vector (finite) of *future outputs* and $\mathbf{y}_p(t)$ a random vector of *past outputs*, then the projection of the "future output data onto the past output data" $\mathcal{P}_{y_f|y_p}$ is invoked by applying the *projection operator* onto the past output data space to the future output data.

This idea of projecting a vector onto a subspace spanned by another vector can be extended to projecting a row space of a matrix onto the row space of another matrix. [19]-[23] Invoking oblique projections of the row space of future data $\mathcal{Y}_f$ onto the row space of past data $\mathcal{Y}_p$ enables us to extract both the extended observability matrix as well as the estimated state vectors by applying a singular value decomposition (*SVD*) operation, that is, (see Refer. 18 for details)

$$\mathcal{P}_{\mathcal{Y}_f|\mathcal{Y}_p} = \mathcal{O}_k \hat{\mathcal{X}}_k = \underbrace{\left(U_{N_x} \Sigma_{N_x}^{1/2}\right)}_{\mathcal{O}_{N_x}} \underbrace{\left((\Sigma'_{N_x})^{1/2} V'_{N_x}\right)}_{\hat{\mathcal{X}}_k} \tag{23}$$

where U_{N_x} and V'_{N_x} are the respective left and right orthogonal matrices of the *SVD* performed on a data matrix [21].

This technique also requires a "shifted" projection $\mathcal{P}_{\mathcal{Y}_f^-|\mathcal{Y}_p^+}$ to extract the model. Here the operator projects shifted future data $\mathcal{Y}_f^-$ as a row and incorporates it into the past output data array such that $\mathcal{Y}_p \rightarrow \mathcal{Y}_p^+$. This projection, coupled with the first enables the extraction of estimated states, since it has been shown that [19]

$$\mathcal{P}_{\mathcal{Y}_f|\mathcal{Y}_p} \;=\; \mathcal{O}_k \times \hat{\mathcal{X}}_k \qquad \text{and} \qquad \mathcal{P}_{\mathcal{Y}_f^-|\mathcal{Y}_p^+} \;=\; \mathcal{O}_{k-1} \times \hat{\mathcal{X}}_{k+1} \qquad \text{[Projections]} \tag{24}$$

where $\mathcal{O}_{k-1}$ is the observability matrix with the last block row removed.

With this in mind, *both* states can be extracted directly from the projections using pseudo-inversion ($\#$) to obtain

$$\hat{\mathcal{X}}_k \;=\; \mathcal{O}_k^{\#} \times \mathcal{P}_{\mathcal{Y}_f|\mathcal{Y}_p} = \mathcal{O}_k \times \hat{\mathcal{X}}_k \qquad \text{and} \qquad \hat{\mathcal{X}}_{k+1} \;=\; \mathcal{O}_{k-1}^{\#} \times \mathcal{P}_{\mathcal{Y}_f^-|\mathcal{Y}_p^+} = \mathcal{O}_{k-1} \times \hat{\mathcal{X}}_{k+1} \qquad \text{[States]} \tag{25}$$

With these states of a so-called Kalman filter [21] now available from the *SVD* and pseudo-inversions, the underlying "batch" state-space (innovations) model can be defined as

$$\begin{aligned} \hat{\mathcal{X}}_{k+1} &= A\,\hat{\mathcal{X}}_k \;+\; B\,\mathcal{U}_{k|k} + \xi_{\omega_k} \\ \hat{\mathcal{Y}}_{k|k} &= C\,\hat{\mathcal{X}}_k \;+\; D\,\mathcal{U}_{k|k} + \xi_{\nu_k} \end{aligned} \tag{26}$$

and the residuals or equivalently innovations sequence and its covariance are defined by

$$\xi := \begin{bmatrix} \xi_{\omega_k} \\ -- \\ \xi_{\nu_k} \end{bmatrix}; \quad \text{and} \quad R_{\xi\xi} := E\{\xi\xi'\} = E\left\{ \begin{bmatrix} \xi_{\omega_k} \\ -- \\ \xi_{\nu_k} \end{bmatrix} \begin{bmatrix} \xi_{\omega_k} & | & \xi_{\nu_k} \end{bmatrix}' \right\} \tag{27}$$

More compactly,

$$\underbrace{\begin{bmatrix} \hat{\mathcal{X}}_{k+1} \\ --- \\ \hat{\mathcal{Y}}_{k|k} \end{bmatrix}}_{\text{known}} = \begin{bmatrix} A & | & B \\ - & - & - \\ C & | & D \end{bmatrix} \underbrace{\begin{bmatrix} \hat{\mathcal{X}}_k \\ --- \\ \mathcal{U}_{k|k} \end{bmatrix}}_{\text{known}} + \begin{bmatrix} \xi_{\omega_k} \\ --- \\ \xi_{\nu_k} \end{bmatrix} \tag{28}$$

which can be solved as an estimation problem providing a *least-squares solution* as:

$$\begin{bmatrix} \hat{A} & | & \hat{B} \\ - & - & - \\ \hat{C} & | & \hat{D} \end{bmatrix} = \left(\begin{bmatrix} \hat{\mathcal{X}}_{k+1} \\ --- \\ \hat{\mathcal{Y}}_{k|k} \end{bmatrix} \begin{bmatrix} \hat{\mathcal{X}}_k \\ --- \\ \mathcal{U}_{k|k} \end{bmatrix}' \right) \left(\begin{bmatrix} \hat{\mathcal{X}}_k \\ --- \\ \mathcal{U}_{k|k} \end{bmatrix} \begin{bmatrix} \hat{\mathcal{X}}_k \\ --- \\ \mathcal{U}_{k|k} \end{bmatrix}' \right)^{-1} \tag{29}$$

with the corresponding "least-squares" residual (innovations) covariances estimated by

$$\hat{R}_{\xi\xi} = \begin{bmatrix} K R_{ee} K' & | & K R_{ee}^{1/2} \\ - & - & - \\ (K R_{ee}^{1/2})' & | & R_{ee} \end{bmatrix} \tag{30}$$

leading to

$$\begin{aligned} \hat{R}_{ee} &\approx R_{\upsilon\upsilon}^{e} && \text{[Innovations Covariance]} \\ \hat{K} &\approx R_{\omega\upsilon}^{e} \hat{R}_{ee}^{-1/2} && \text{[Kalman Gain]} \end{aligned} \tag{31}$$

Thus, the *full-solution* of the stochastic realization problem, $\Sigma_{\text{INV}} = \{\hat{A}, \hat{B}, \hat{C}, \hat{D}, R^e_{\omega\omega}, R^e_{\omega v}, R^e_{vv}\}$, is obtained through the solution of these least-squares relations using the *N4SID*-method [19]. The is summarized below and subsequently applied to measured data to extract an acoustic test object model.

Summarizing, the subspace algorithm (*N4SID*) is accomplished using the following steps (see Fig. 40:

- *Create* the block Hankel matrix from the measured output sequence, $\{\mathbf{y}(t)\}$;
- *Calculate* the projection matrices $\mathcal{P}_{\mathcal{Y}_f|\mathcal{Y}_p}$ and $\mathcal{P}_{\mathcal{Y}_f^-|\mathcal{Y}_p^+}$ (shifted);
- *Perform* the *SVD* of the projection matrix to obtain the extended observability and estimated state vector $\mathcal{X}_k$;
- *Perform* the *SVD* of the "shifted" projection matrix to obtain the "shifted" observability and estimated state vector $\mathcal{X}_{k+1}$;
- *Extract* the system matrix $\hat{A}$ and output $\hat{C}$ matrices by solving the corresponding least-squares problem;
- *Calculate* the reversed controllability matrix $\overleftarrow{\overline{\mathcal{C}}}_{AB}$;
- *Extract* the input transmission matrix $\hat{\overline{B}}_e$;
- *Extract* the input/output matrix $\hat{D}$ from estimated output covariance $\hat{\Lambda}_0$;
- *Estimate* the set of noise source covariances $\{R^e_{WW}, R^e_{VV}, R^e_{WV}\}$ using the estimated least-squares residuals covariance $\hat{R}_{\xi\xi}$; and
- *Calculate* R_{ee} and K_p from the least-squares residuals.

completing the algorithm.

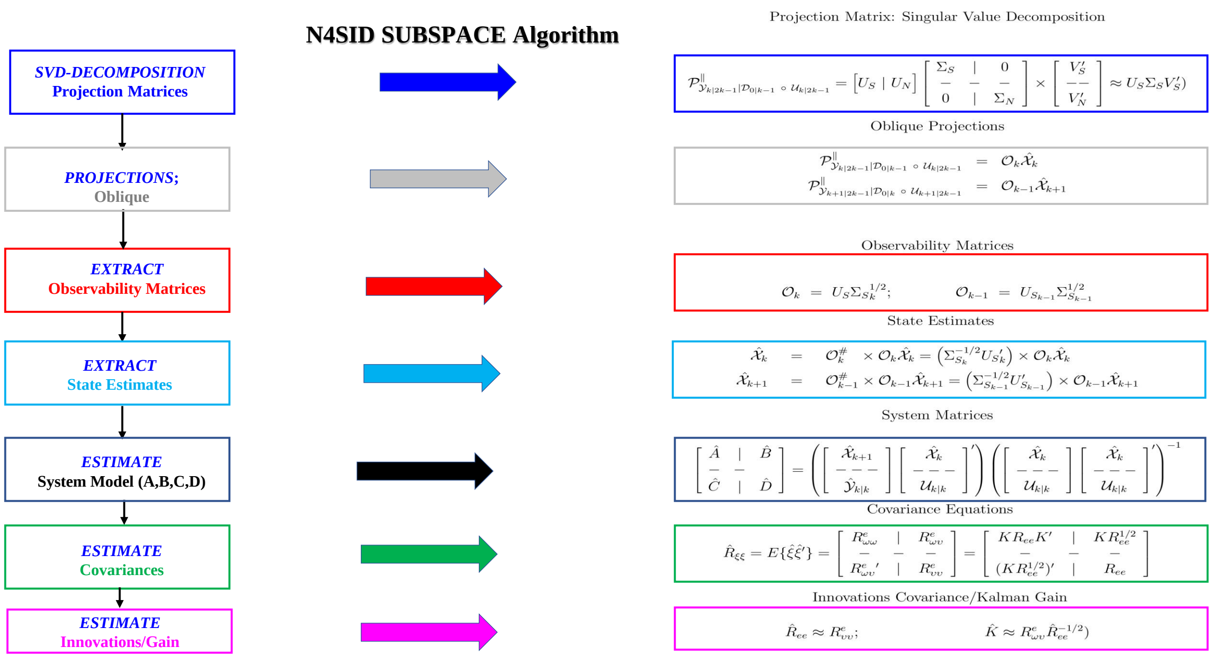

Figure 40: Numerical Algorithm for Subspace Identification (N4SID) Algorithm: Diagram and Calculations.

APPENDIX B: Deconvolution Estimation: Wiener Least-Squares Processor

The classical method of solving the deconvolution problem is based an optimal (Wiener) filter design minimizing a mean-squared error criterion [14]. It is possible to derive the processor by using the commutative property of the convolution relation, that is,

$$y(t) = \mathcal{H}(t) * u(t) = u(t) * \mathcal{H}(t) \tag{32}$$

The deconvolution problem is concerned with obtaining the "optimal" estimate of the excitation $u(t)$ given $(\{y(t)\}, \{\mathcal{H}(t)\})$. The estimator is found by minimizing the mean-squared error criterion given by

$$\min_{\mathbf{u}} \mathcal{J}(t) = \frac{1}{2} E\{e^2(t)\} \tag{33}$$

where $e(t) := y(t) - \hat{y}(t)$ and

$$\hat{y}(t) = u(t) * \mathcal{H}(t) = \sum_{i=0}^{N_u} u(i)\mathcal{H}(t-i) \tag{34}$$

Following the standard approach of differentiating the cost and setting the result to zero, leads to the so-called *orthogonality condition* given by

$$\frac{\partial}{\partial u(j)} \mathcal{J}(t) = E\{e(t)\frac{\partial e(t)}{\partial u(j)}\} = 0; \quad \text{for} \quad j = 0, \cdots, N_u \tag{35}$$

the error gradient is therefore

$$\frac{\partial e(t)}{\partial u(j)} = \frac{\partial}{\partial u(j)} (y(t) - \hat{y}(t)) = \frac{\partial}{\partial u(j)} \left(y(t) - \sum_{i=0}^{N_u} u(i)\mathcal{H}(t-i) \right) = \mathcal{H}(t-j) \tag{36}$$

Substituting, the set of *normal equations* evolve as

$$\sum_{i=0}^{N_u} u(i) R_{\mathcal{H}\mathcal{H}}(i-j) = r_{y\mathcal{H}}(j) \quad \text{for } j = 0, \ldots, N_u \tag{37}$$

Expanding this equation gives the set of vector-matrix relations

$$\mathbf{R}_{\mathcal{H}\mathcal{H}}(N_u)\mathbf{u}(N_u) = \mathbf{r}_{y\mathcal{H}}(N_u) \tag{38}$$

where $\mathbf{R}_{\mathcal{H}\mathcal{H}} \in \mathcal{R}^{(N_u+1)\times(N_u+1)}$ is Toeplitz and can be solved in "batch" form as

$$\hat{\mathbf{u}}(N_u) = \mathbf{R}_{\mathcal{H}\mathcal{H}}^{-1}(N_u)\mathbf{r}_{y\mathcal{H}}(N_u) \tag{39}$$

or recursively with the well-known Levinson-Wiggins-Robinson (*LWR*) recursion [14].

Summarizing, the batch deconvolution approach is:

Criterion: $J = E\{e^2(t)\}$

Models:

Measurement: $y(t) = \mathcal{H}(t) * u(t)$

Signal: $s(t) = -\sum_{i=0}^{N_u} u_i \mathcal{H}(t-i)$

Noise: R_{ee}

Algorithm: $\hat{\mathbf{u}} = \mathbf{R}_{\mathcal{H}\mathcal{H}}^{-1} \mathbf{r}_{y\mathcal{H}}$

Quality: $R_{ee}(N_u)$

APPENDIX C: Spectrogram Estimation: Recursive ARMA Processor

In this appendix we discuss a recursive-in-time approach to instantaneous spectral estimation or spectrogram enabling us to produce the desired spectrogram (amplitude vs. time vs. frequency) for event detection of transient signals [14], [26]. We can parametrically model the noisy measurement data by an instantaneous time-frequency representation specified by an autoregressive moving average *ARMA* scalar model. This model takes the general difference equation form, $ARMA(N_a,N_c)$ given by

$$A(q^{-1},t)y(t) = C(q^{-1},t)\varepsilon(t) \tag{40}$$

for the enhanced measurement, $y(t)$, contaminated with zero-mean, white Gaussian noise, $\varepsilon \sim \mathcal{N}(0, \sigma_s \varepsilon^2)$, with the corresponding instantaneous polynomials at the instant t defined by

$$\begin{aligned} A(q^{-1},t) &= 1 + a_1(t)q^{-1} + \cdots + a_{N_a}(t)q^{-N_a} \\ C(q^{-1},t) &= c_o + c_1(t)q^{-1} + \cdots + c_{N_c}(t)q^{-N_c} \end{aligned} \tag{41}$$

Here the backward shift or delay operator is defined by, $q^{-i}y(t) := y(t-i)$ and therefore, we can write Eq. 40 simply as

$$y(t) = -\sum_{k=1}^{N_a} a_k(t)y(t-k) + \sum_{k=0}^{N_c} c_k(t)\varepsilon(t-k) \tag{42}$$

If we take the DFT of the difference equation, then we obtain the *instantaneous transfer function* (ignoring stochastic aspect)

$$H(e^{j2\pi f},t) = \frac{Y(e^{j2\pi f},t)}{\mathrm{E}(e^{j2\pi f},t)} = \frac{C(e^{j2\pi f},t)}{A(e^{j2\pi f},t)}, \tag{43}$$

or more appropriately the corresponding *instantaneous power spectrum* defined by

$$S(f,t) := \left|H(e^{j2\pi f},t)\right|^2 = \left|\frac{C(e^{j2\pi f},t)}{A(e^{j2\pi f},t)}\right|^2 \tag{44}$$

So we see that if we use the parametric $ARMA(N_a,N_c)$ representation of the enhanced measurement signal and transform it to the spectral domain, then we can obtain the instantaneous spectral estimate.

There are a wealth of adaptive ARMA algorithms available in the literature ([14], [26]), but since we are primarily interested in estimating the spectrum at each time instant, we confine our choices to those that are recursive-in-time enabling us to achieve our goal without the loss of temporal resolution evolving from window-based methods such as the short-time Fourier transform [14]. Recall that recursive-in-time algorithms take on the following generic form:

$$\underline{\hat{\Theta}}(t+1) = \underline{\hat{\Theta}}(t) + \underline{K}(t)e(t) \qquad \text{[parameter update]}$$

$$e(t) = y(t) - \hat{y}(t) = y(t) - \underline{\varphi}'(t)\underline{\hat{\Theta}}(t) \qquad \text{[prediction error]}$$

$$\underline{\varphi}(t) \equiv [y(t-1) \quad \cdots \quad y(t-N_a-1) \mid \hat{e}(t) \quad \cdots \quad \hat{e}(t-N_c)]\,, \tag{45}$$

$$\underline{\hat{\Theta}}(t) \equiv [-\hat{a}_1(t-1) \quad \cdots \quad -\hat{a}_{N_a}(t-N_a-1) \mid \hat{c}_o(t) \quad \cdots \quad \hat{c}_{N_c}(t-N_c)]'$$

with $\underline{K}(t)$ the gain or weighting vector and the $\wedge$ symbol defining the "best" (minimum error variance) estimate at the specified time. There are also many variations and forms of this basic recursion [14], but here we limit our application to the recursive prediction error method (*RPEM*) based on a local Gauss-Newton optimization method.

Criterion: $\mathcal{J}(\underline{\theta}(t)) = E\{e^2(t)\}$

Models:

Signal: $s(t) = -\sum_{i=1}^{N_a} a_i y(t-i)$

Measurement: $y(t) = s(t) + n(t)$

Noise: $\hat{n}(t) = \sum_{i=0}^{N_c} c_i \epsilon(t-i)$

Initial conditions: $\underline{\Theta}(0)$

Algorithm: $\Theta(t) = \Theta(t-1) + \mu K(t)e(t)$

Quality: $P(t) = (I - K(t)\phi\prime(t))P(t-1)/\lambda(t)$

References

[1] R. Wiggins and E. Robinson,"Recursive solution to the multichannel filtering problem," J. Geophys. Res. 70(8), 1885-1891 (1965).

[2] E. Robinson and S. Treitel, *Geophysical Signal Analysis* (Prentice-Hall,Englewood Cliffs,NJ,1980).

[3] L. Dicus, "Impulse response estimation with underwater explosive charge acoustic signals," J. Acoust. Soc. Am. 70 (1), 122-133, 1981.

[4] J. Walsh, "On limitations of minimum mean-square error deconvolution in deriving impulse responses of rooms," J. Acoust. Soc. Am. 77 (2), pp 547-556, 1985.

[5] C-Y. Chi and W-T Chen, "An adaptive maximum-likelihood deconvolution algorithm," Signal Proc. 24, pp 149-163, 1991.

[6] M. Tanter, J-L Thomas and M. Fink, "Time reversal and the inverse filter" J. Acoust. Soc. Am. 108 (1), 223-234, 2000.

[7] T. Gallot, S. Catheline, P. Roux and M. Campillo, "A passive inverse filter for Green's function retrieval" J. Acoust. Soc. Am. Exp. Letters, 131 (1), EL21-EL26, 2012.

[8] J. Kormylo and J. Mendel, "Maximum-likelihood deconvolution", *IEEE Trans. Geosci. Remote Sensing*, Vol. GE-21, pp. 72-82, 1983.

[9] J. Mendel, *Maximum-likelihood Deconvolution: a Journey Into Model-based Signal Processing*, (Springer,NY,1990).

[10] J. Candy, R. Ziolkowski, and K. Lewis, "Transient wave estimation: a multichannel deconvolution application," J. Acoust. Society Amer., Vol. 88 (5), pp 2235-2247, 1990.

[11] P. Mignerey and S. Finette, "Multichannel deconvolution of an acoustic transient in an oceanic waveguide," J. Acoust. Society Amer., Vol. 92 (1), pp 351-364, 1992.

[12] T. Olofsson and T. Stepinski, "Maximum a posteriori deconvolution of ultrasonic signals using multiple transducers," J. Acoust. Soc. Am. 107 (6), 3276-3288, 2000.

[13] E. J. Sullivan, *Model-Based Processing for Underwater Acoustic Arrays.* (Springer,NY,2015.

[14] J. Candy, *Model-Based Signal Processing*, (John Wiley/IEEE Press,Hoboken NJ,2006).

[15] W. Gawronski, *Advanced Structural Dynamics and Active Control of Structures.* (Springer,London,UK, 2004).

[16] M. Aoki, *State Space Modeling of Time Series.* 2^{nd}-Ed. (Springer-Verlag,London,UK,1990).

[17] J. Candy, K. Fisher, J. Case, B. Illingworth, K. Craft, *Excitation Recovery Problem: A Model-Based Approach to Multichannel Deconvolution*, LLNL-Report, LLNL-TR-813769, 2020.

[18] S. Jensen and B. Markowicz, *Transportation Vibration Characterization of a 48' Air ride Trailer with 1500 lbs. Mass Load*, LLNL Internal Memo, 2016.

[19] P. van Overschee and B. De Moor, "N4SID: Numerical algorithms for State Space Subspace System Identification." Automatica, vol 30, pp. 75-93, 1994.

[20] P. van Overschee and B. De Moor, *Subspace Identification for Linear Systems: Theory, Implementation, Applications*. (Kluwer Academic,Boston,MA,1996).

[21] J. Candy, *Model-Based Processing: An Applied Subspace Approach*, (John Wiley,Hoboken,NJ,2019).

[22] T. Katayama, *Subspace Methods for System Identification*. (Springer,London,UK,2005).

[23] M. Verhaegen and V. Verdult, *Filtering and System Identification: A Least-Squares Approach*. (Cambridge University Press,Cambridge,UK,2007).

[24] J. Candy, S. Franco, E. Ruggiero, M. Emmons, I. Lopez and L. Stoops, "Anomaly detection for a vibrating structure: A subspace identification/tracking approach, *J. Acoust. Soc. Am.*, Vol. 142, (2), pp. 680-696, 2017.

[25] E. Reynders, "System identification methods for (operational) modal analysis: review and comparison," *Archives of Comp. Methods Engr.*, Vol. 19 (1), pp. 51-124, 2012.

[26] L. J. Ljung, *System Identification: Theory for the User*. 2^{nd}-Ed., (Prentice-Hall,Englewood Cliffs,NJ,1999).